Elemental composition, iron mineralogy and solubility of anthropogenic and natural mineral dust aerosols in Namibia: a case study analysis from the AEROCLO-sA campaign

Paola Formenti[1*], Chiara Giorio[2,3], Karine Desboeufs[1], Alexander Zherebker[2], Marco Gaetani[4], Clarissa Baldo[5], Gautier Landrot[6], Simona Montebello[2,7], Servanne Chevaillier[1], Sylvain Triquet[1], Guillaume Siour[5], Claudia Di Biagio[1], Francesco Battaglia[1], Jean-François Doussin[5], Anais Feron[1,$], Andreas Namwoonde[8], and Stuart Piketh[9]

[1] Université Paris Cité and Univ. Paris Est Creteil, CNRS, LISA, F−75013 Paris, France
[2] Yusuf Hamied Department of Chemistry, University of Cambridge, Lensfield Road, Cambridge, CB2 1EW, United Kingdom
[3] Dipartimento di Scienze Chimiche, Università degli Studi di Padova, 35131 Padova, Italy
[4] Classe di Scienze Tecnologie e Società, Scuola Universitaria Superiore IUSS, 27100, Pavia, Italia
[5] Univ Paris Est Creteil and Université Paris Cité, CNRS, LISA, F−94010 Créteil, France
[6] Synchrotron SOLEIL, L'Orme des Merisiers, Saint-Aubin, France
[7] Department of Engineering 'Enzo Ferrari', University of Modena and Reggio Emilia, 41125 Modena, Italy
[8] Sam Nujoma Marine and Coastal Resources Research Centre, University of Namibia, Henties Bay, Namibia
[9] NorthWest University, Potchefstroom, South Africa
[$] now at INRAE

*Correspondence to: paola.formenti@lisa.ipsl.fr

Table S1. Ancillary instrumentation relevant to this publication

Observables	Instrumentation	Details of sampling	Frequency of acquisition
Wind speed/ direction, air temperature, relative humidity	Compact weather station (model CE155N, CE157N, BA711, Cimel Electronique, Paris, France)	10 m above ground level, extendable mast on the roof of the PEGASUS facility.	5-minute
Particle number size distribution (0.25-32 µm optical diameter)	Optical particle counter (OPC, model 1.109, GRIMM Inc., DE)	Flow rate = 1.2 L min^{-1}	6-sec resolution

Table S2. List of standard material and reference spectra used for the least-square deconvolution of the XANES spectra. The first four lines report the identification numbers and details of preparation of the six standards that were prepared for these work. They consisted of as round pellets of 10 mm^2 in a matrix of Boron Nitride (BN, molar mass 24.819 g mol^{-1}) prepared using an automatic hydraulic Press (Atlas Power T8, Specac), available at the chemistry laboratory at SOLEIL, operated at a pressure of 5 Tons. The dilution rate of the standard compounds was adjusted using the ABSORBIX (X-ray absorbance and fluorescence self-absorption calculations) software to optimize the absolute and relative values of the Fe-absorption edge (Michalowicz et al., 2009). The Fe mass and total pellet mass are reported in the last column (the total pellet mass is in brackets). The pellets were analyzed sequentially in transmission mode.

ID	CAS number	Stoichiometric formula	Dilution rate in the pellet (%)	Total surface mass concentration (g cm^{-2})	Mass of standard, µg
Ref4	13268-42-3	$(NH_4)_3[Fe(C_2O_4)_3]$ $3H_2O$	20	0.125	19.75 (97.5)
Ref6	166897-40-1	$Fe_2(C_2O_4)_3$ $6H_2O$	12	0.125	11.70 (97.5)
Ref1	6047-25-2	$Fe{\cdot}(C_2O_4){\cdot}2(H_2O)$	10	0.125	9.75 (97.5)
Ref15	1345-25-1	FeO	5	0.110	4.29 (97.5)

Table S3. Summary statistics of elemental and water-soluble ionic concentrations measured during the campaign in the TSP and PM_1 fractions. The second column indicates the number of samples for which values were above the minimum quantification limit (MQL). The arithmetic means and standard deviations (SD) are reported in ng m^{-3}.

	TSP			PM1		
	Mean	**SD**	**Number of samples**	**Mean**	**Std**	**Number of samples**
Cl	37338	18647	36	1070	721	28
S	3069	1359	36	429	146	28
Ca	1744	771	36	94	70	28
Fe	582	412	36	38	39	23
Na	22829	11169	36	611	360	28
Mg	2812	1284	36	89	48	28
Al	582	426	36	30	27	28
Si	2575	1448	36	208	83	28
P	18	8	36	< MQL	< MQL	< MQL
K	1254	550	36	52	25	28
Ti	57	41	36	4	3	23
Mn	15	11	36	10	12	17
Zn	13	7	36	< MQL	< MQL	< MQL
Cr	7	4	34	< MQL	< MQL	< MQL
V	11	5	36	< MQL	< MQL	< MQL
Ba	6	5	7	< MQL	< MQL	< MQL
Co	8	4	36	< MQL	< MQL	< MQL
Cu	13	5	36	< MQL	< MQL	< MQL
Nd	13	6	36	< MQL	< MQL	< MQL
Ni	10	5	36	< MQL	< MQL	< MQL
Sr	54	30	35	< MQL	< MQL	< MQL
Cd	197	156	25	< MQL	< MQL	< MQL
As	74	52	34	< MQL	< MQL	< MQL
Pb	40	30	35	< MQL	< MQL	< MQL
Na^+	22155	10743	35	819	414	28
K^+	1184	618	35	56	21	25
Ca^{2+}	1658	750	35	62	18	17
Mg^{2+}	3679	2012	35	89	45	26
Cl^-	38894	20550	35	906	620	28
SO_4^{2-}	9066	4272	35	1083	352	28
NH_4^+	260	128	35	239	83	28
MSA	61	26	25	46	16	25
NO_3^-	965	687	35	100	29	28
F^-	4330	2317	13	301	166	28
Br^-	170	154	27	<MQL	<MQL	< MQL
PO_4^{3-}	39	12	4	<MQL	<MQL	< MQL
oxalate	125	50	27	69	19	28
formate	405	274	23	18	5	11
acetate	32	11	9	20	9	27
OC	3213	1459	36	117	57	28
EC	271	234	28	14	9	9

Table S4. The list of AI_{con}-based formulae classes with atomic constraints

Formulae class	O/C	H/C	AI_{con}
Lipids	< 0.3	≥ 1.5**	-
N-containing saturated compounds (N-saturated)	-	≥ 1.5*	-
Aliphatics	≥ 0.3	≥ 1.5**	-
Unsaturated (low O/C)	< 0.5	< 1.5	< 0.5
Unsaturated (high O/C)	≥ 0.5	< 1.5	< 0.5
Aromatic (low O/C)	< 0.5	-	≥ 0.5 and < 0.67
Aromatic (high O/C)	≥ 0.5	-	≥ 0.5 and < 0.67
Condensed (low O/C)	< 0.5	-	≥ 0.67
Condensed (high O/C)	≥ 0.5	-	≥ 0.67

* N > 0; ** N = 0

Figure S1. Surface wind direction (top) and wind direction (bottom) measured during the AEROCLO-sA campaign in Henties Bay.

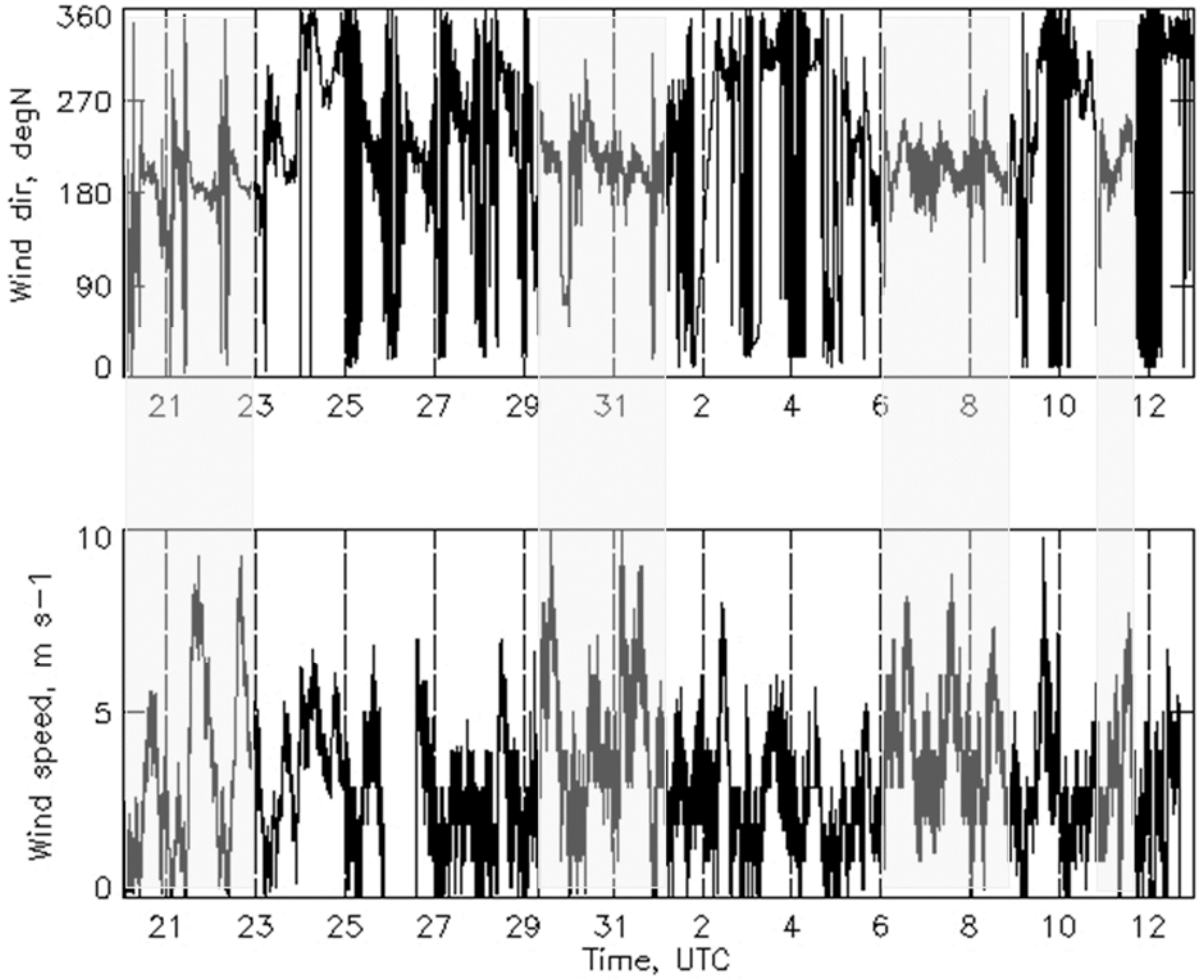

Figure S2. CAMS geopotential height at 700 hPa (m) and aerosol optical depth at 550 nm, from 22 August to 12 September 2017. The red dot indicates the location of Henties Bay.

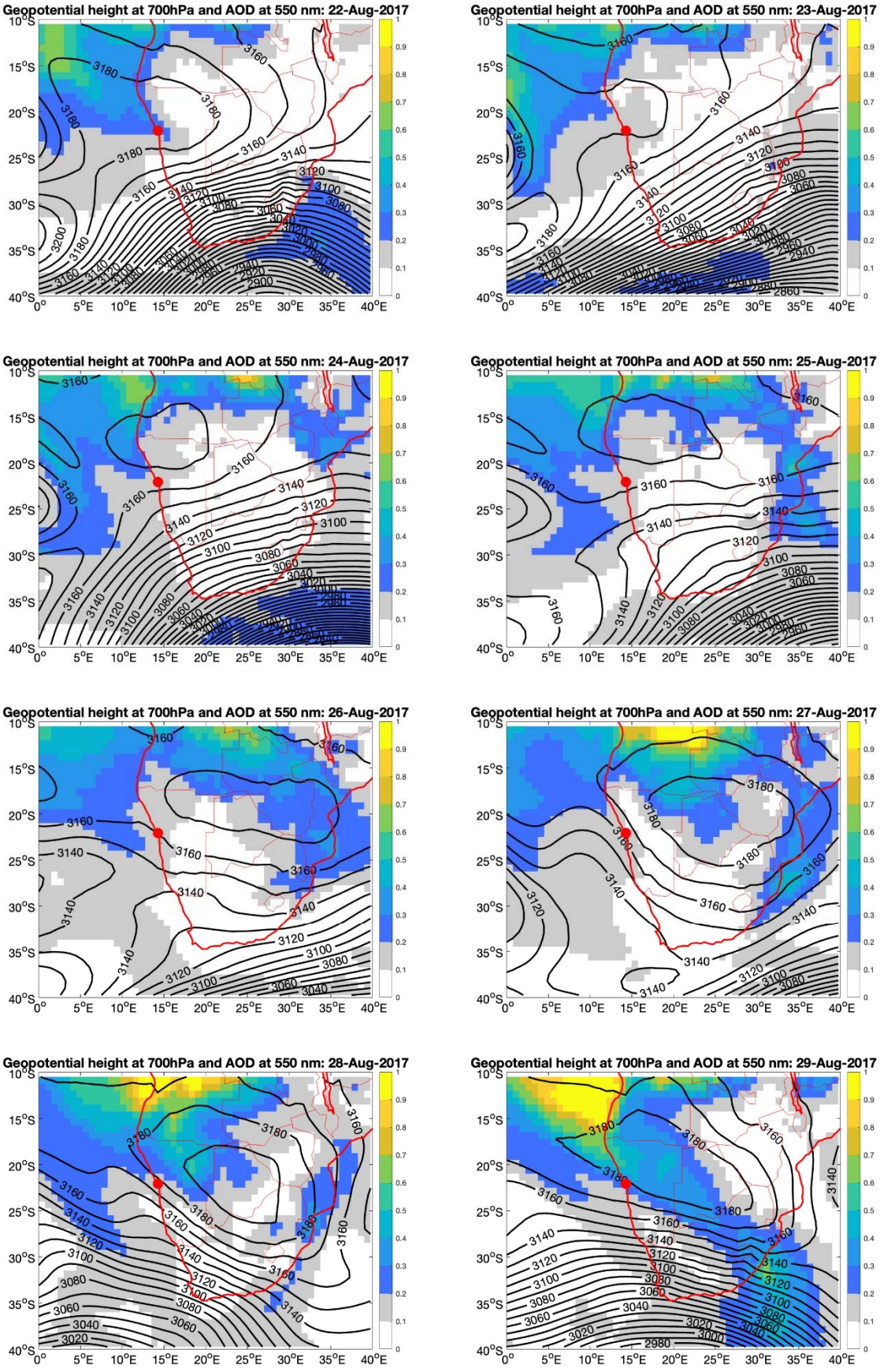

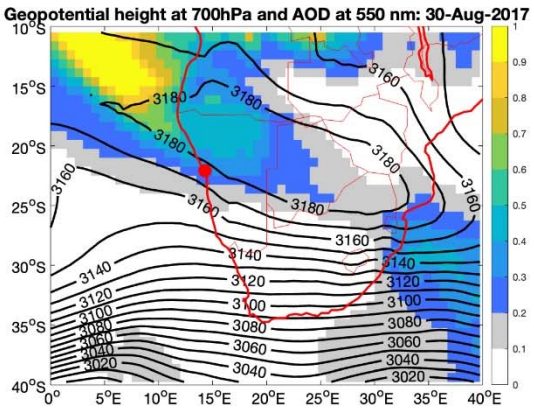
Geopotential height at 700hPa and AOD at 550 nm: 30-Aug-2017

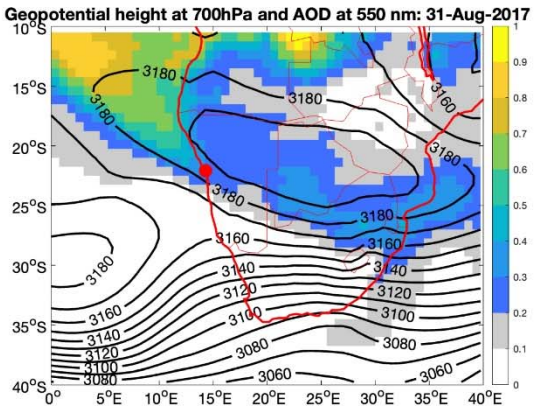
Geopotential height at 700hPa and AOD at 550 nm: 31-Aug-2017

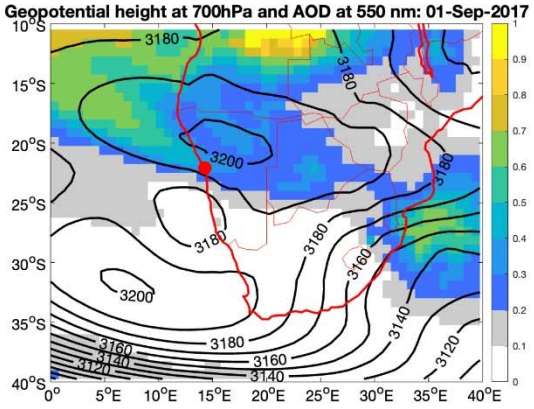
Geopotential height at 700hPa and AOD at 550 nm: 01-Sep-2017

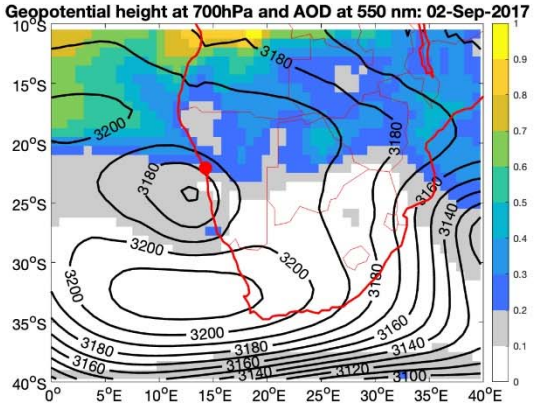
Geopotential height at 700hPa and AOD at 550 nm: 02-Sep-2017

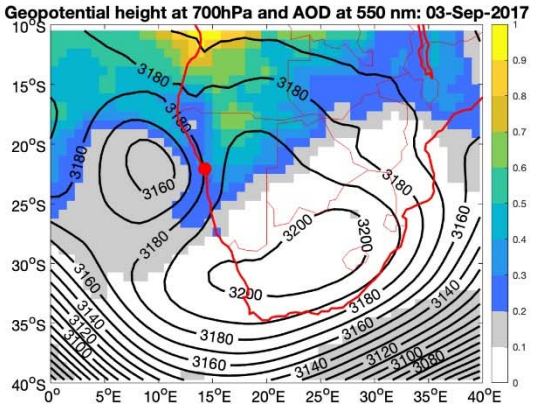
Geopotential height at 700hPa and AOD at 550 nm: 03-Sep-2017

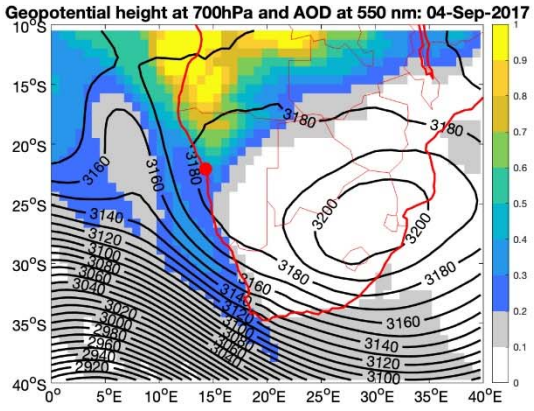
Geopotential height at 700hPa and AOD at 550 nm: 04-Sep-2017

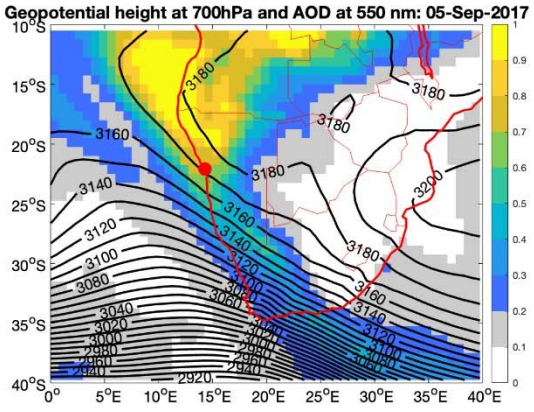
Geopotential height at 700hPa and AOD at 550 nm: 05-Sep-2017

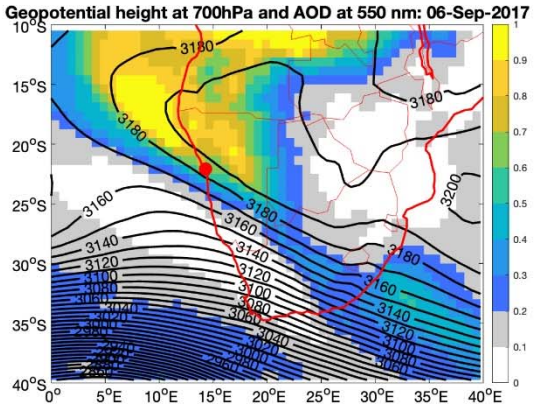
Geopotential height at 700hPa and AOD at 550 nm: 06-Sep-2017

60

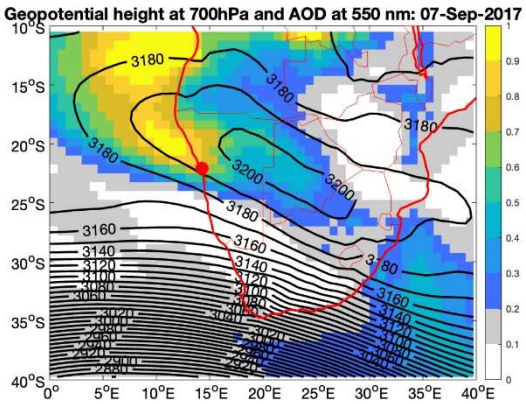
Geopotential height at 700hPa and AOD at 550 nm: 07-Sep-2017

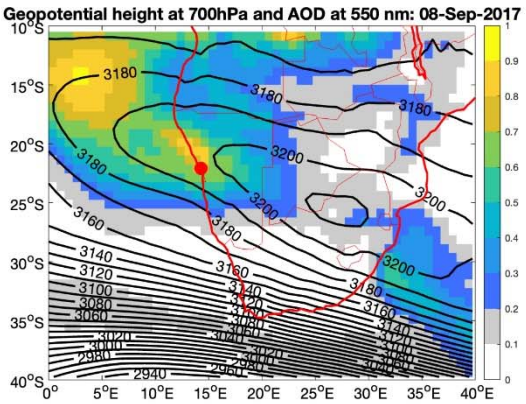
Geopotential height at 700hPa and AOD at 550 nm: 08-Sep-2017

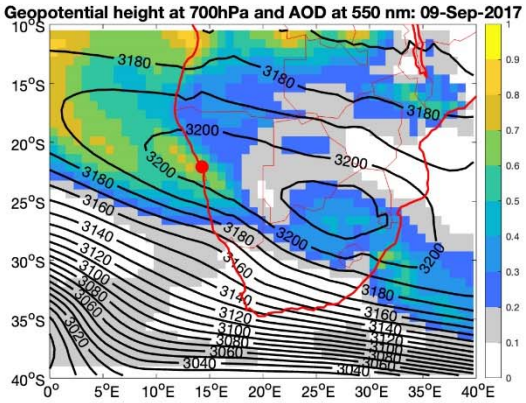
Geopotential height at 700hPa and AOD at 550 nm: 09-Sep-2017

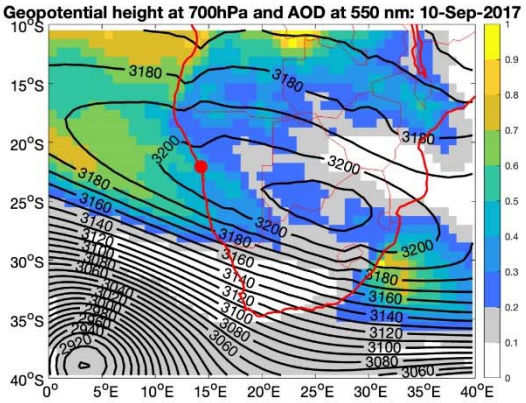
Geopotential height at 700hPa and AOD at 550 nm: 10-Sep-2017

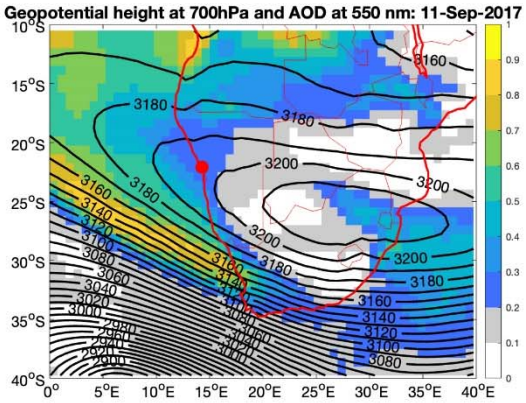
Geopotential height at 700hPa and AOD at 550 nm: 11-Sep-2017

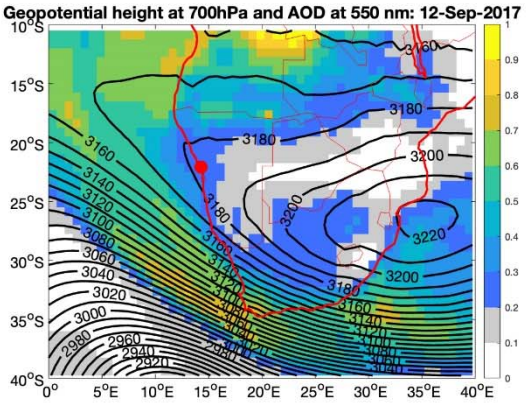
Geopotential height at 700hPa and AOD at 550 nm: 12-Sep-2017

61
62

Figure S3. Air mass back-trajectories calculated with 9 km (left) and 50 km (right) spatial resolution

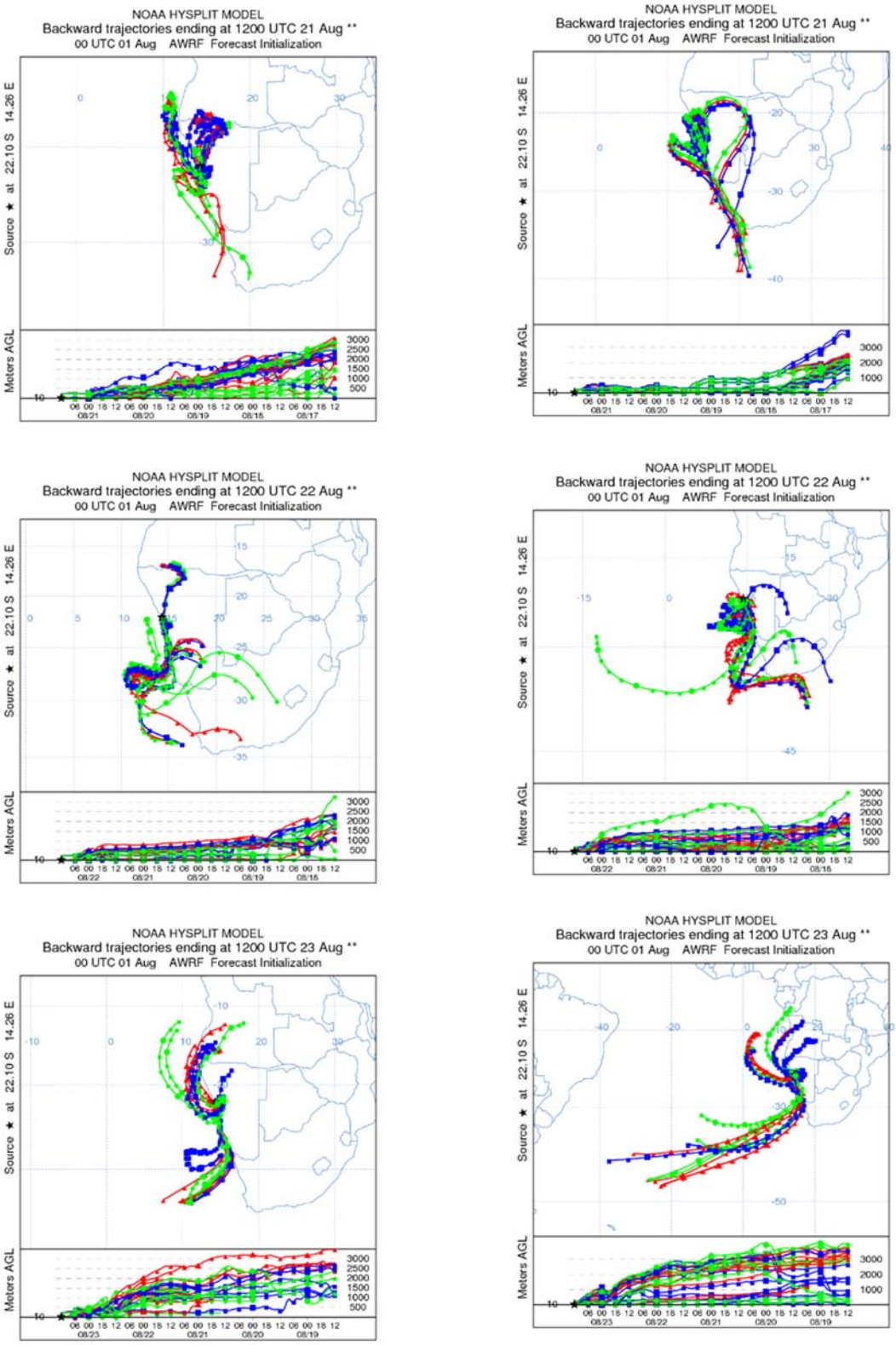

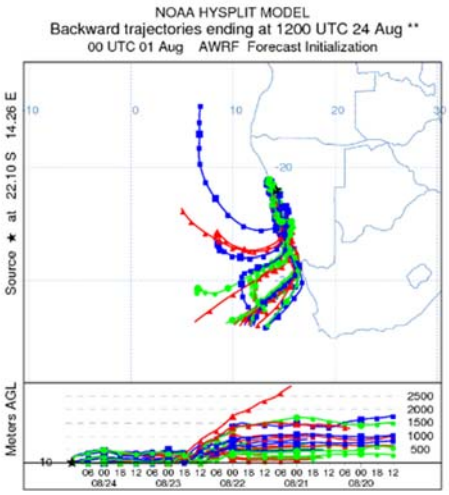
NOAA HYSPLIT MODEL
Backward trajectories ending at 1200 UTC 24 Aug **
00 UTC 01 Aug AWRF Forecast Initialization
Source ★ at 22.10 S 14.26 E
Meters AGL

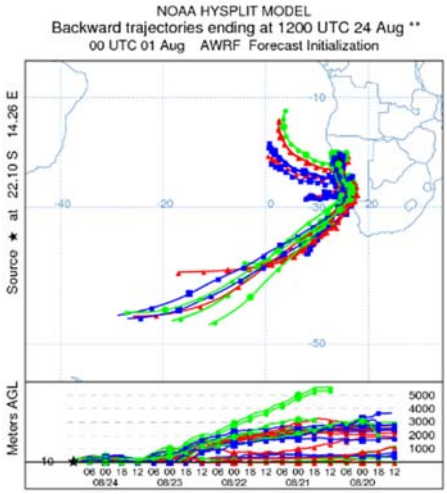
NOAA HYSPLIT MODEL
Backward trajectories ending at 1200 UTC 24 Aug **
00 UTC 01 Aug AWRF Forecast Initialization
Source ★ at 22.10 S 14.26 E
Meters AGL

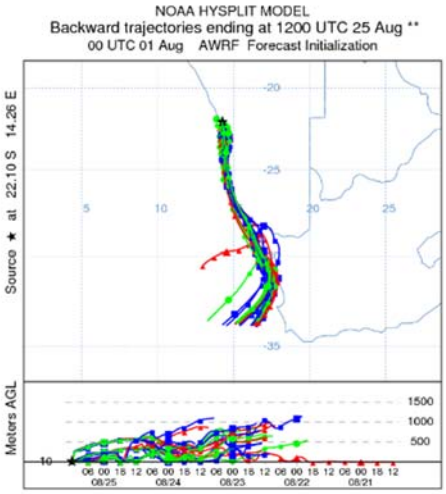
NOAA HYSPLIT MODEL
Backward trajectories ending at 1200 UTC 25 Aug **
00 UTC 01 Aug AWRF Forecast Initialization
Source ★ at 22.10 S 14.26 E
Meters AGL

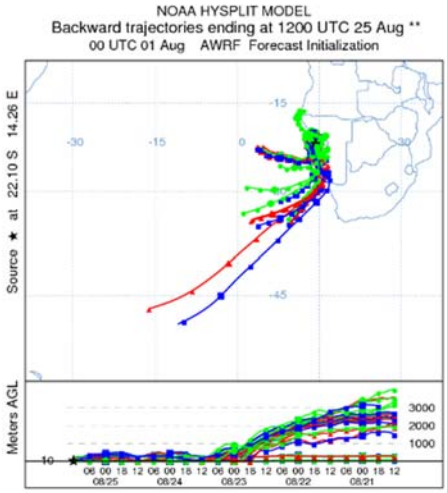
NOAA HYSPLIT MODEL
Backward trajectories ending at 1200 UTC 25 Aug **
00 UTC 01 Aug AWRF Forecast Initialization
Source ★ at 22.10 S 14.26 E
Meters AGL

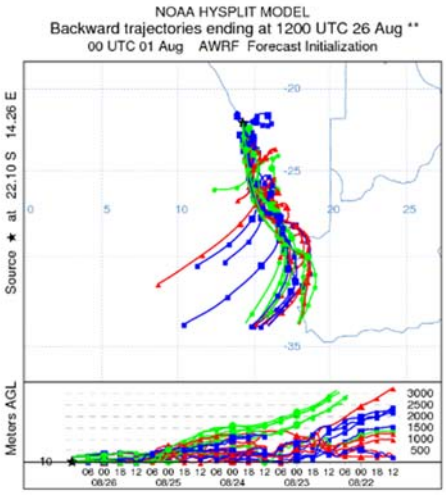
NOAA HYSPLIT MODEL
Backward trajectories ending at 1200 UTC 26 Aug **
00 UTC 01 Aug AWRF Forecast Initialization
Source ★ at 22.10 S 14.26 E
Meters AGL

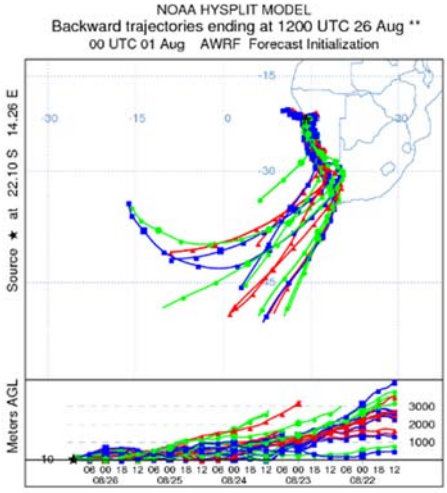
NOAA HYSPLIT MODEL
Backward trajectories ending at 1200 UTC 26 Aug **
00 UTC 01 Aug AWRF Forecast Initialization
Source ★ at 22.10 S 14.26 E
Meters AGL

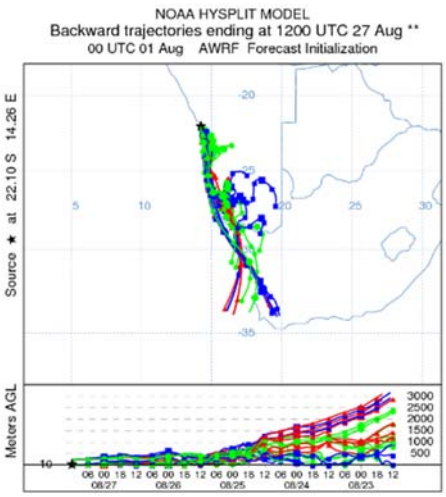
NOAA HYSPLIT MODEL
Backward trajectories ending at 1200 UTC 27 Aug **
00 UTC 01 Aug AWRF Forecast Initialization
Source ★ at 22.10 S 14.26 E
Meters AGL

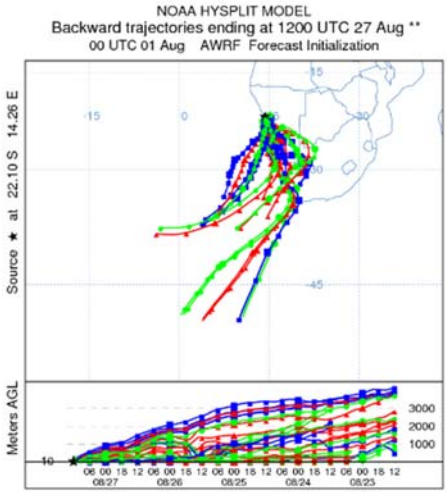
NOAA HYSPLIT MODEL
Backward trajectories ending at 1200 UTC 27 Aug **
00 UTC 01 Aug AWRF Forecast Initialization
Source ★ at 22.10 S 14.26 E
Meters AGL

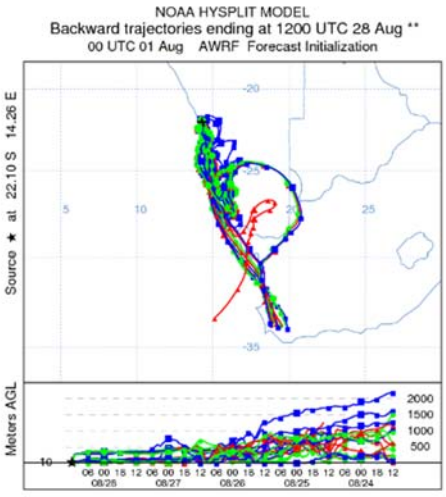
NOAA HYSPLIT MODEL
Backward trajectories ending at 1200 UTC 28 Aug **
00 UTC 01 Aug AWRF Forecast Initialization
Source ★ at 22.10 S 14.26 E
Meters AGL

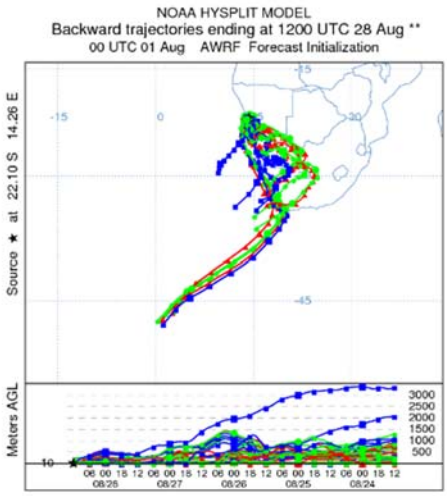
NOAA HYSPLIT MODEL
Backward trajectories ending at 1200 UTC 28 Aug **
00 UTC 01 Aug AWRF Forecast Initialization
Source ★ at 22.10 S 14.26 E
Meters AGL

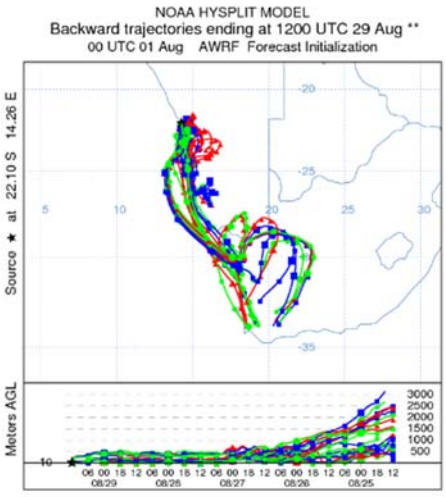
NOAA HYSPLIT MODEL
Backward trajectories ending at 1200 UTC 29 Aug **
00 UTC 01 Aug AWRF Forecast Initialization
Source ★ at 22.10 S 14.26 E
Meters AGL

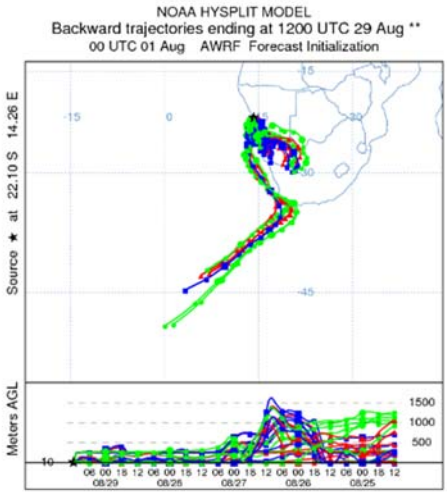
NOAA HYSPLIT MODEL
Backward trajectories ending at 1200 UTC 29 Aug **
00 UTC 01 Aug AWRF Forecast Initialization
Source ★ at 22.10 S 14.26 E
Meters AGL

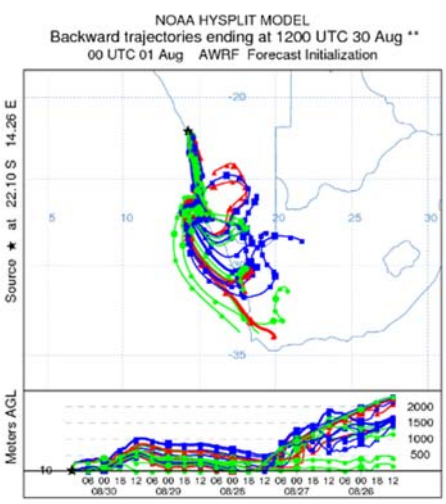
NOAA HYSPLIT MODEL
Backward trajectories ending at 1200 UTC 30 Aug **
00 UTC 01 Aug AWRF Forecast Initialization
Source ★ at 22.10 S 14.26 E
Meters AGL

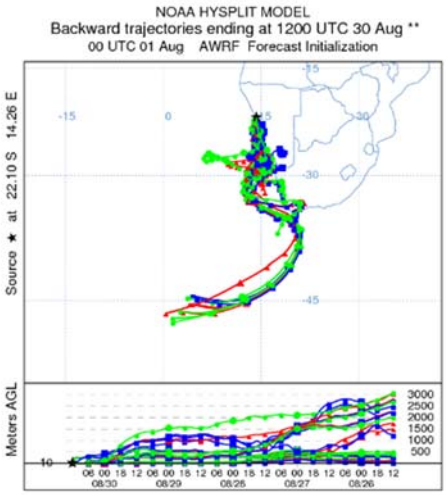
NOAA HYSPLIT MODEL
Backward trajectories ending at 1200 UTC 30 Aug **
00 UTC 01 Aug AWRF Forecast Initialization
Source ★ at 22.10 S 14.26 E
Meters AGL

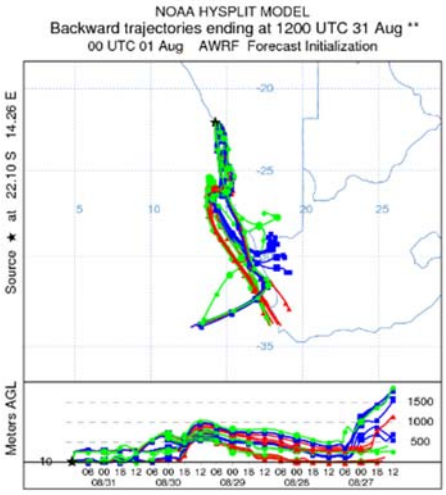
NOAA HYSPLIT MODEL
Backward trajectories ending at 1200 UTC 31 Aug **
00 UTC 01 Aug AWRF Forecast Initialization
Source ★ at 22.10 S 14.26 E
Meters AGL

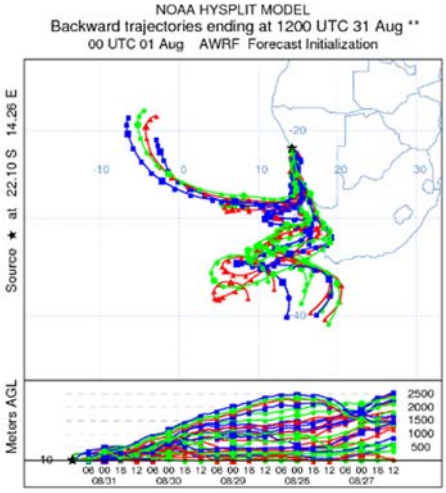
NOAA HYSPLIT MODEL
Backward trajectories ending at 1200 UTC 31 Aug **
00 UTC 01 Aug AWRF Forecast Initialization
Source ★ at 22.10 S 14.26 E
Meters AGL

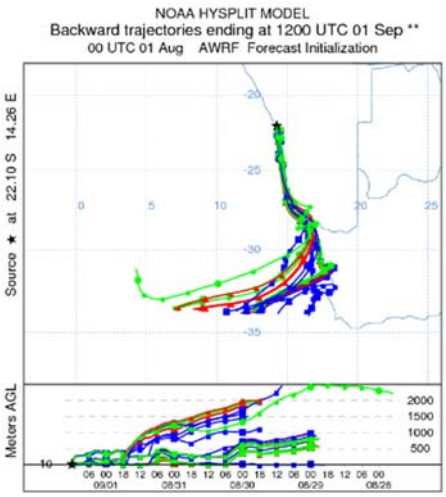
NOAA HYSPLIT MODEL
Backward trajectories ending at 1200 UTC 01 Sep **
00 UTC 01 Aug AWRF Forecast Initialization
Source ★ at 22.10 S 14.26 E
Meters AGL

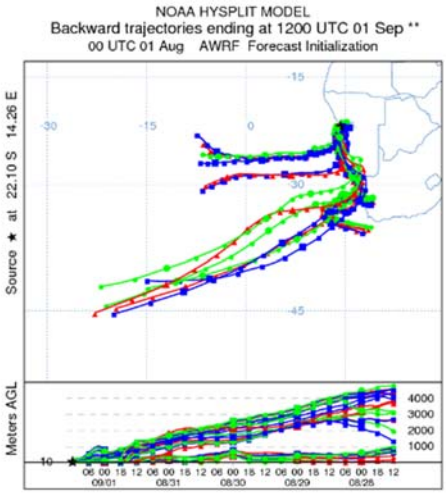
NOAA HYSPLIT MODEL
Backward trajectories ending at 1200 UTC 01 Sep **
00 UTC 01 Aug AWRF Forecast Initialization
Source ★ at 22.10 S 14.26 E
Meters AGL

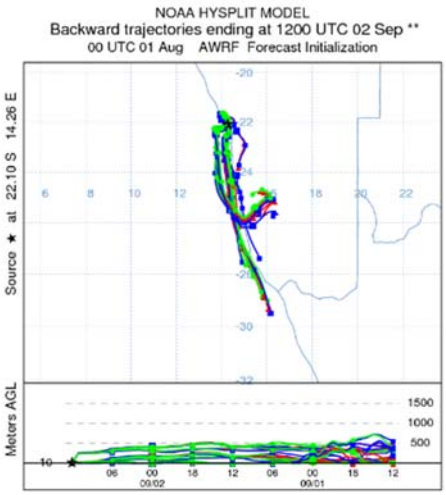
NOAA HYSPLIT MODEL
Backward trajectories ending at 1200 UTC 02 Sep **
00 UTC 01 Aug AWRF Forecast Initialization
Source ★ at 22.10 S 14.26 E
Meters AGL

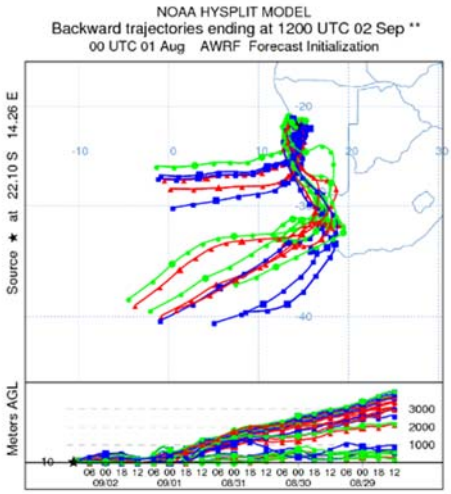
NOAA HYSPLIT MODEL
Backward trajectories ending at 1200 UTC 02 Sep **
00 UTC 01 Aug AWRF Forecast Initialization
Source ★ at 22.10 S 14.26 E
Meters AGL

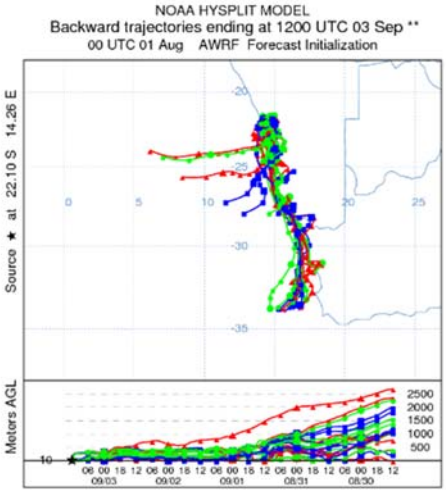
NOAA HYSPLIT MODEL
Backward trajectories ending at 1200 UTC 03 Sep **
00 UTC 01 Aug AWRF Forecast Initialization
Source ★ at 22.10 S 14.26 E
Meters AGL

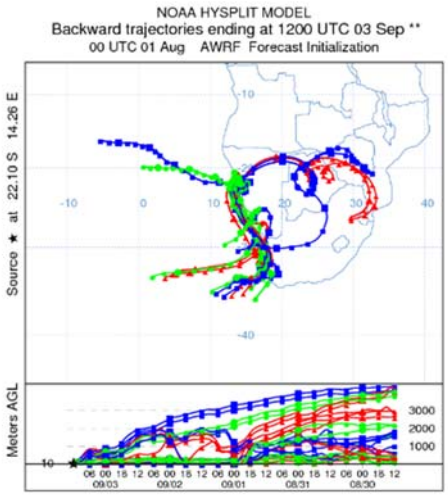
NOAA HYSPLIT MODEL
Backward trajectories ending at 1200 UTC 03 Sep **
00 UTC 01 Aug AWRF Forecast Initialization
Source ★ at 22.10 S 14.26 E
Meters AGL

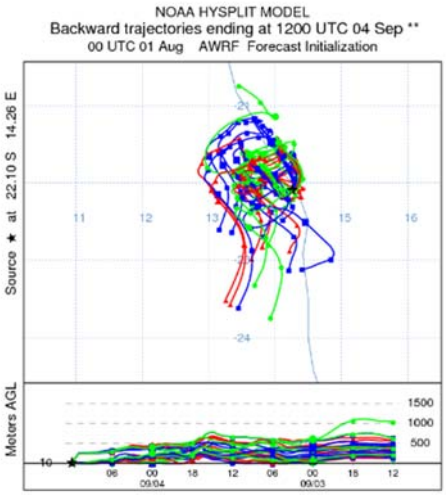
NOAA HYSPLIT MODEL
Backward trajectories ending at 1200 UTC 04 Sep **
00 UTC 01 Aug AWRF Forecast Initialization
Source ★ at 22.10 S 14.26 E
Meters AGL

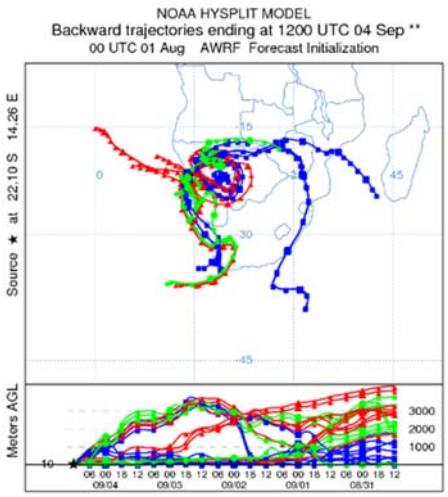
NOAA HYSPLIT MODEL
Backward trajectories ending at 1200 UTC 04 Sep **
00 UTC 01 Aug AWRF Forecast Initialization
Source ★ at 22.10 S 14.26 E
Meters AGL

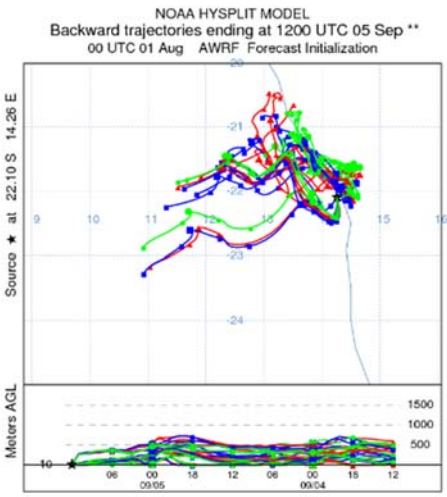
NOAA HYSPLIT MODEL
Backward trajectories ending at 1200 UTC 05 Sep **
00 UTC 01 Aug AWRF Forecast Initialization
Source ★ at 22.10 S 14.26 E
Meters AGL

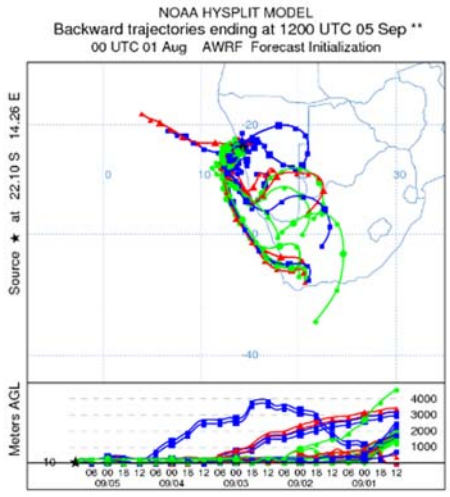
NOAA HYSPLIT MODEL
Backward trajectories ending at 1200 UTC 05 Sep **
00 UTC 01 Aug AWRF Forecast Initialization
Source ★ at 22.10 S 14.26 E
Meters AGL

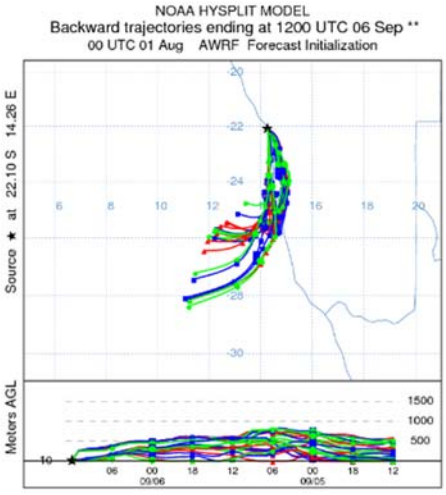
NOAA HYSPLIT MODEL
Backward trajectories ending at 1200 UTC 06 Sep **
00 UTC 01 Aug AWRF Forecast Initialization
Source ★ at 22.10 S 14.26 E
Meters AGL

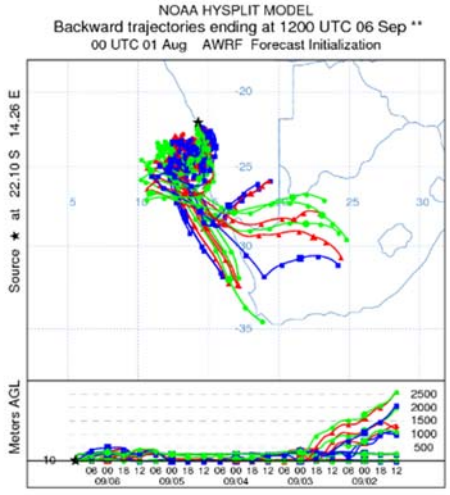
NOAA HYSPLIT MODEL
Backward trajectories ending at 1200 UTC 06 Sep **
00 UTC 01 Aug AWRF Forecast Initialization
Source ★ at 22.10 S 14.26 E
Meters AGL

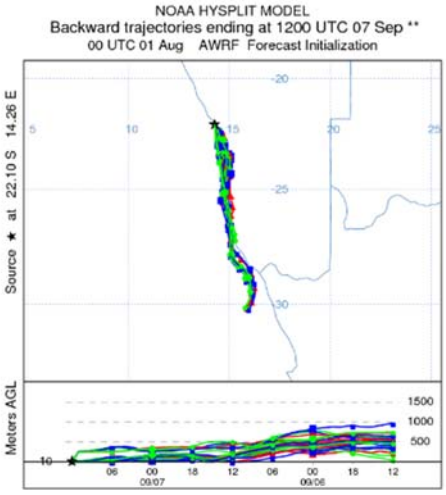
NOAA HYSPLIT MODEL
Backward trajectories ending at 1200 UTC 07 Sep **
00 UTC 01 Aug AWRF Forecast Initialization
Source ★ at 22.10 S 14.26 E
Meters AGL

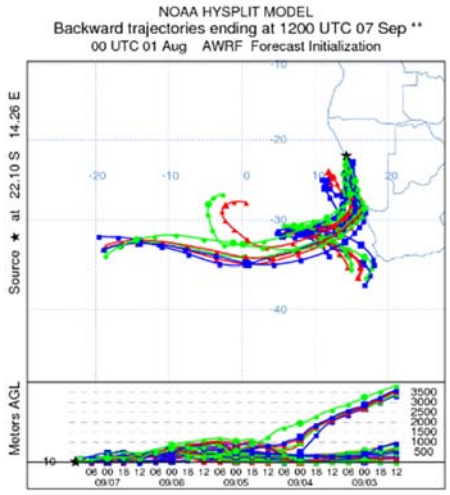
NOAA HYSPLIT MODEL
Backward trajectories ending at 1200 UTC 07 Sep **
00 UTC 01 Aug AWRF Forecast Initialization
Source ★ at 22.10 S 14.26 E
Meters AGL

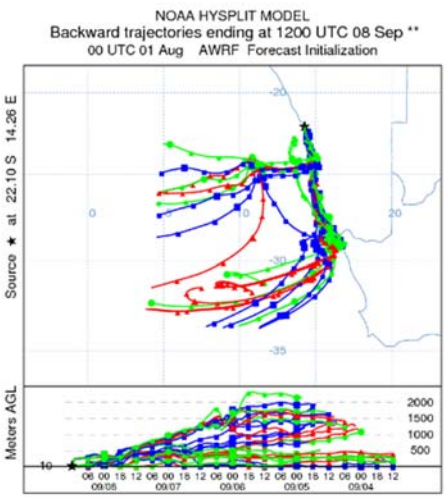
NOAA HYSPLIT MODEL
Backward trajectories ending at 1200 UTC 08 Sep **
00 UTC 01 Aug AWRF Forecast Initialization
Source ★ at 22.10 S 14.26 E
Meters AGL

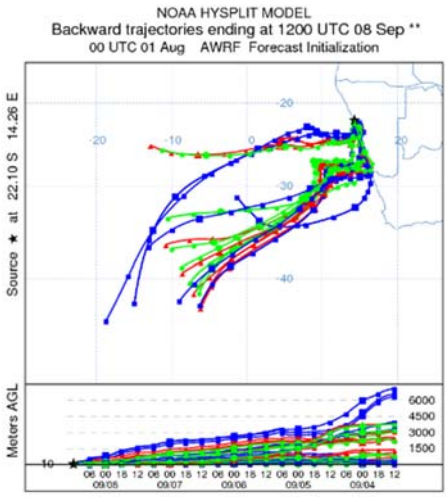
NOAA HYSPLIT MODEL
Backward trajectories ending at 1200 UTC 08 Sep **
00 UTC 01 Aug AWRF Forecast Initialization
Source ★ at 22.10 S 14.26 E
Meters AGL

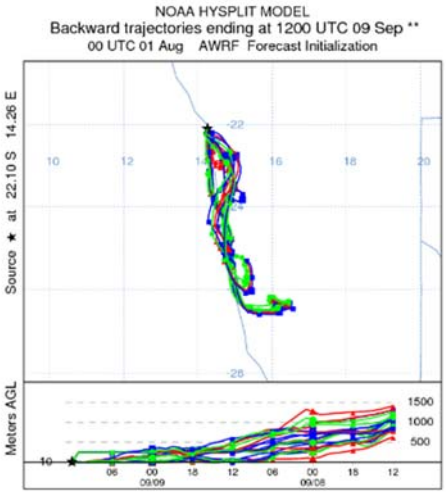
NOAA HYSPLIT MODEL
Backward trajectories ending at 1200 UTC 09 Sep **
00 UTC 01 Aug AWRF Forecast Initialization
Source ★ at 22.10 S 14.26 E
Meters AGL

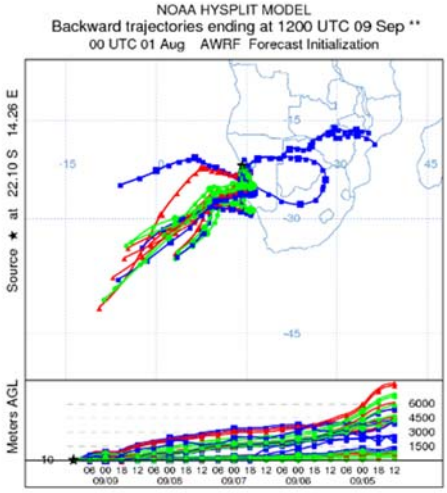
NOAA HYSPLIT MODEL
Backward trajectories ending at 1200 UTC 09 Sep **
00 UTC 01 Aug AWRF Forecast Initialization
Source ★ at 22.10 S 14.26 E
Meters AGL

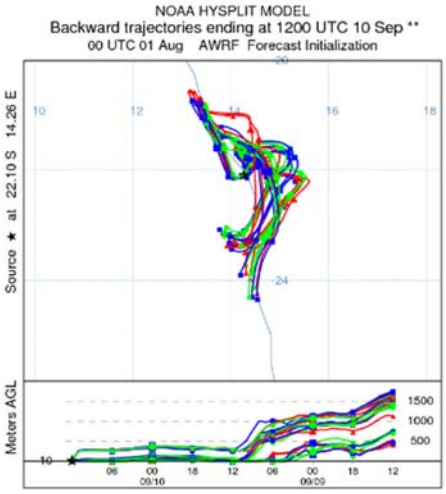
NOAA HYSPLIT MODEL
Backward trajectories ending at 1200 UTC 10 Sep **
00 UTC 01 Aug AWRF Forecast Initialization
Source ★ at 22.10 S 14.26 E
Meters AGL

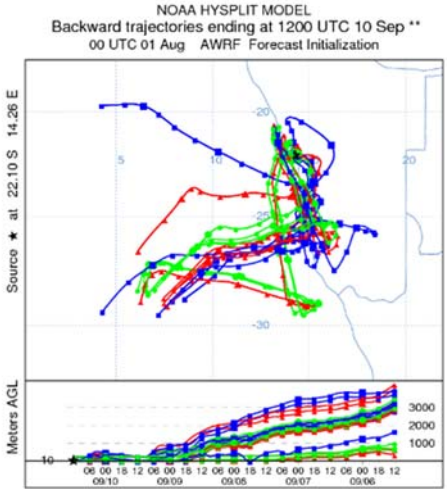
NOAA HYSPLIT MODEL
Backward trajectories ending at 1200 UTC 10 Sep **
00 UTC 01 Aug AWRF Forecast Initialization
Source ★ at 22.10 S 14.26 E
Meters AGL

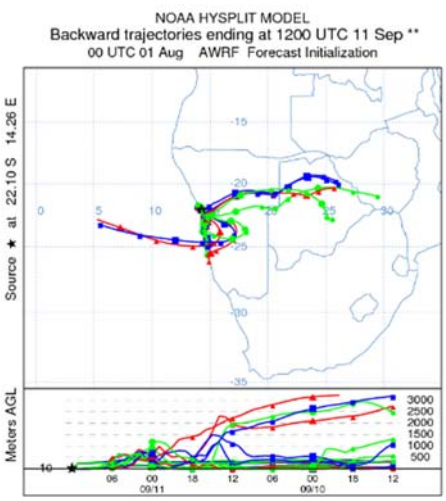
NOAA HYSPLIT MODEL
Backward trajectories ending at 1200 UTC 11 Sep **
00 UTC 01 Aug AWRF Forecast Initialization
Source ★ at 22.10 S 14.26 E
Meters AGL

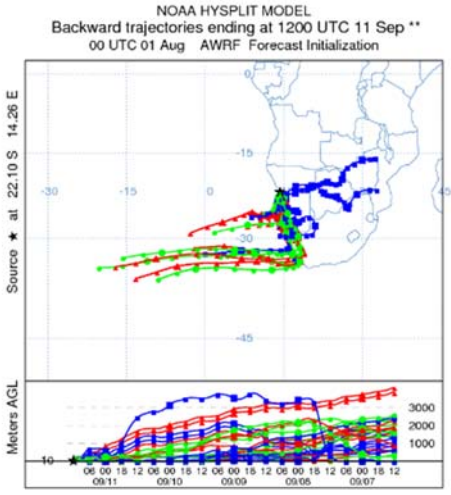
NOAA HYSPLIT MODEL
Backward trajectories ending at 1200 UTC 11 Sep **
00 UTC 01 Aug AWRF Forecast Initialization
Source ★ at 22.10 S 14.26 E
Meters AGL

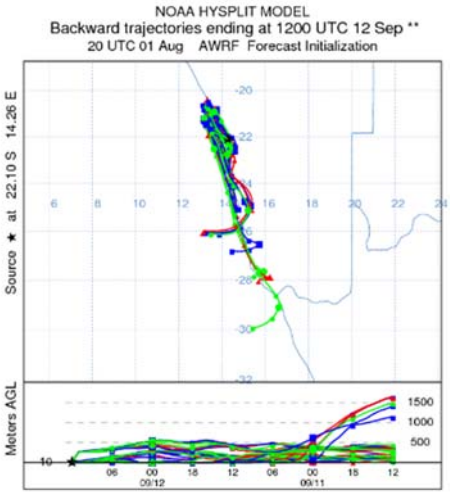
NOAA HYSPLIT MODEL
Backward trajectories ending at 1200 UTC 12 Sep **
20 UTC 01 Aug AWRF Forecast Initialization
Source ★ at 22.10 S 14.26 E
Meters AGL

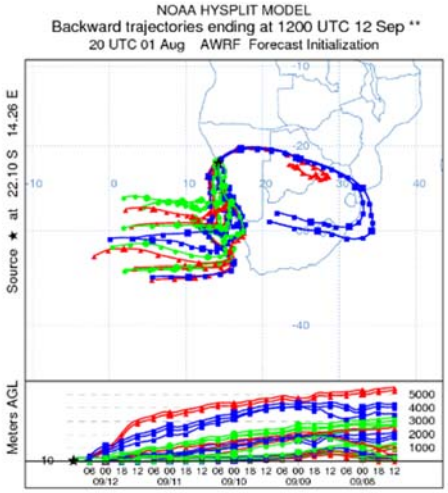
NOAA HYSPLIT MODEL
Backward trajectories ending at 1200 UTC 12 Sep **
20 UTC 01 Aug AWRF Forecast Initialization
Source ★ at 22.10 S 14.26 E
Meters AGL

66
67

Figure S5. Box and whiskers distributions of ratios to Al of various elements measured during the field campaign. Values are sorted according to the meteorological periods P1 to P3. The P3 period is split into two sub-periods (P3a and P3b) to highlight the changes in the particle composition towards the end of the campaign. The box indicates the interquartile range, i.e. the 25th and 75th percentiles, and the line within the box marks the median. The whiskers indicate the quartiles 1.5 times the interquartile range. Points above and below the whiskers indicate outliers outside the 10th and 90th percentiles.

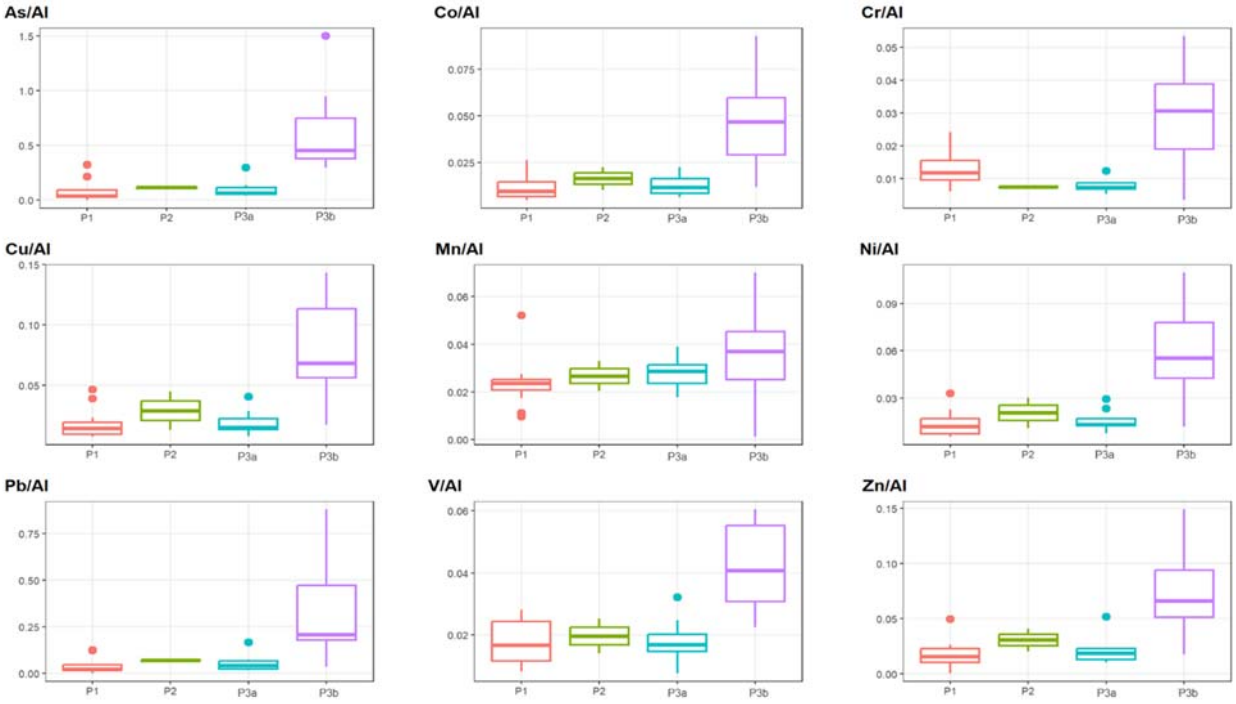

Figure S6. Time series of the coarse particle number concentration (PCN, cm^{-3}) measured by the GRIMM optical sizer operated during the field campaign.

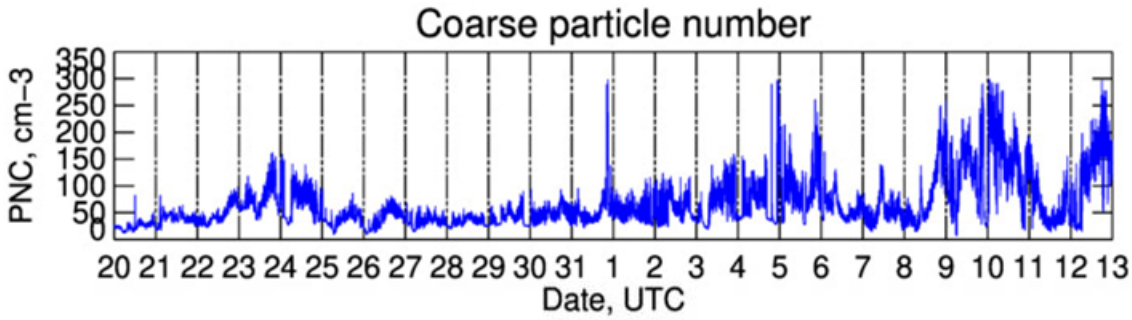

Figure S7. CAMS wind at 10-m (arrows, m s^{-1}) and surface mass mixing ratio (shading, µg kg^{-1}) for (left) mineral dust and (right) sulphate aerosols from 22 August to 12 September 2017. The red dot indicates the location of Henties Bay.

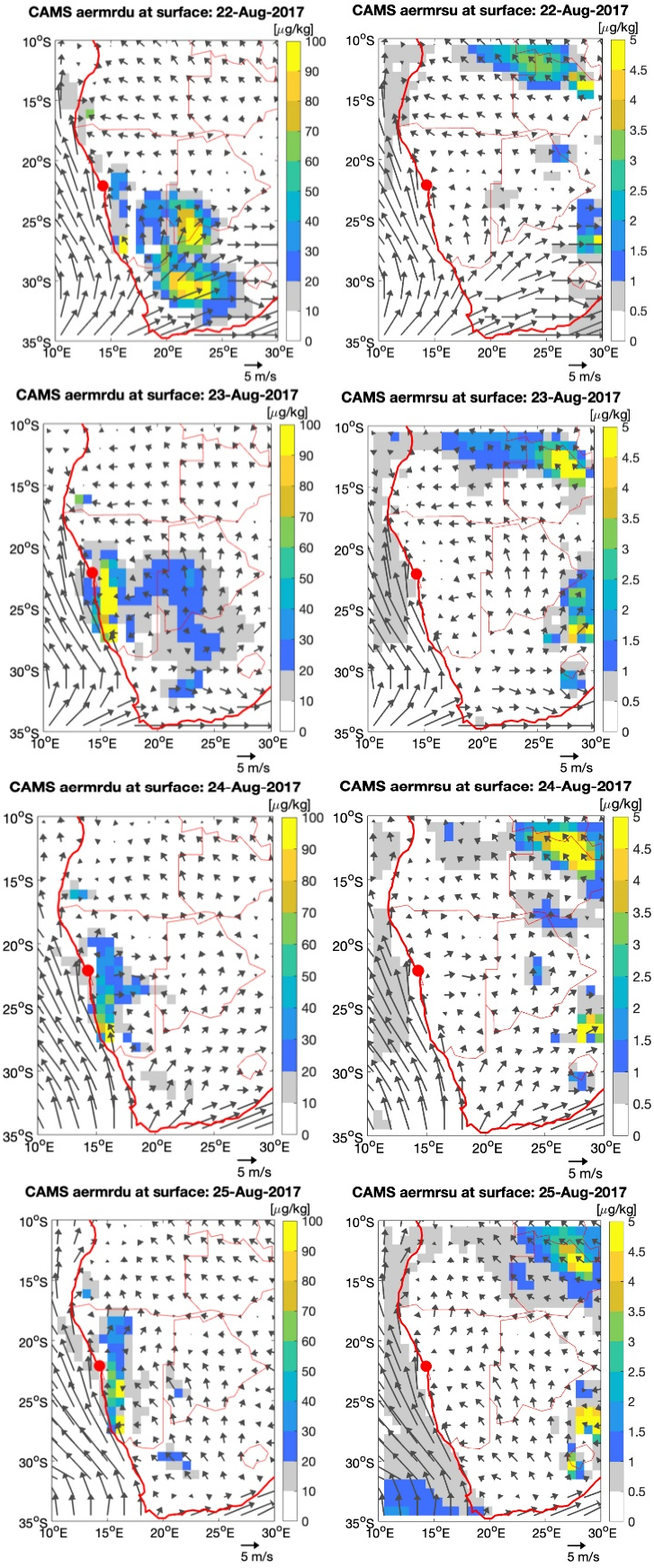

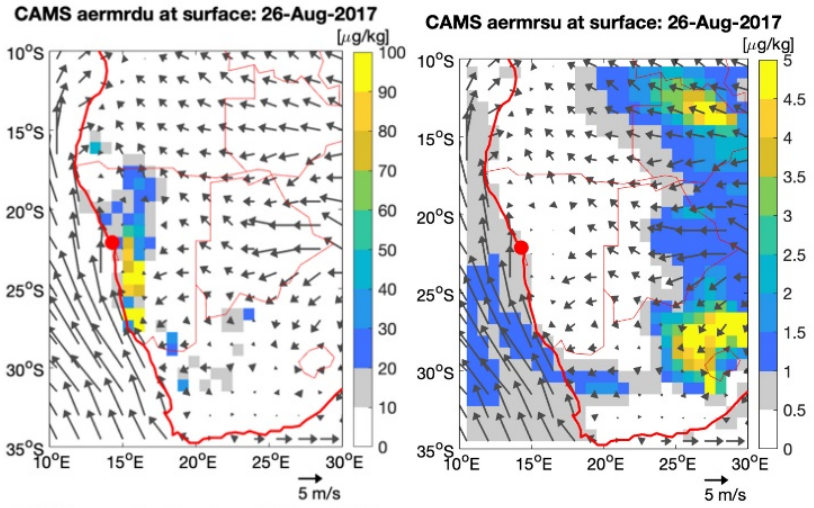
CAMS aermrdu at surface: 26-Aug-2017
[μg/kg]
100
90
80
70
60
50
40
30
20
10
0
10°S
15°S
20°S
25°S
30°S
35°S
10°E
15°E
20°E
25°E
30°E
5 m/s

CAMS aermrsu at surface: 26-Aug-2017
[μg/kg]
5
4.5
4
3.5
3
2.5
2
1.5
1
0.5
0
10°S
15°S
20°S
25°S
30°S
35°S
10°E
15°E
20°E
25°E
30°E
5 m/s

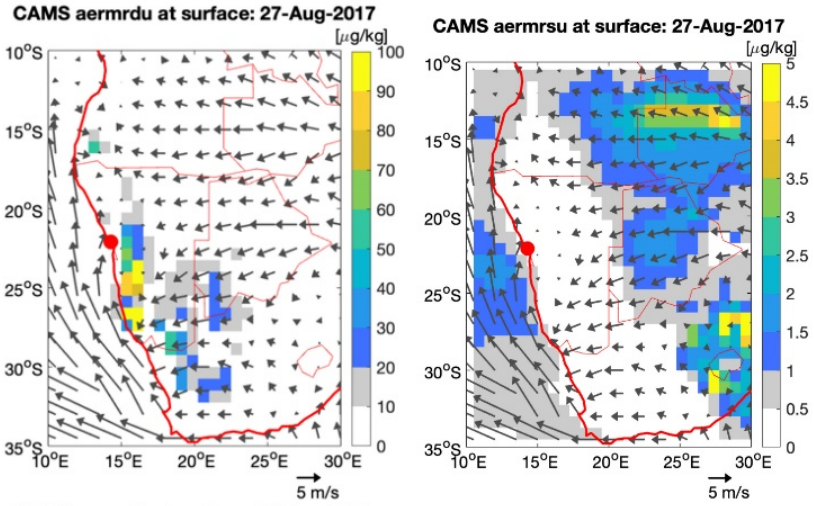
CAMS aermrdu at surface: 27-Aug-2017
[μg/kg]
100
90
80
70
60
50
40
30
20
10
0
10°S
15°S
20°S
25°S
30°S
35°S
10°E
15°E
20°E
25°E
30°E
5 m/s

CAMS aermrsu at surface: 27-Aug-2017
[μg/kg]
5
4.5
4
3.5
3
2.5
2
1.5
1
0.5
0
10°S
15°S
20°S
25°S
30°S
35°S
10°E
15°E
20°E
25°E
30°E
5 m/s

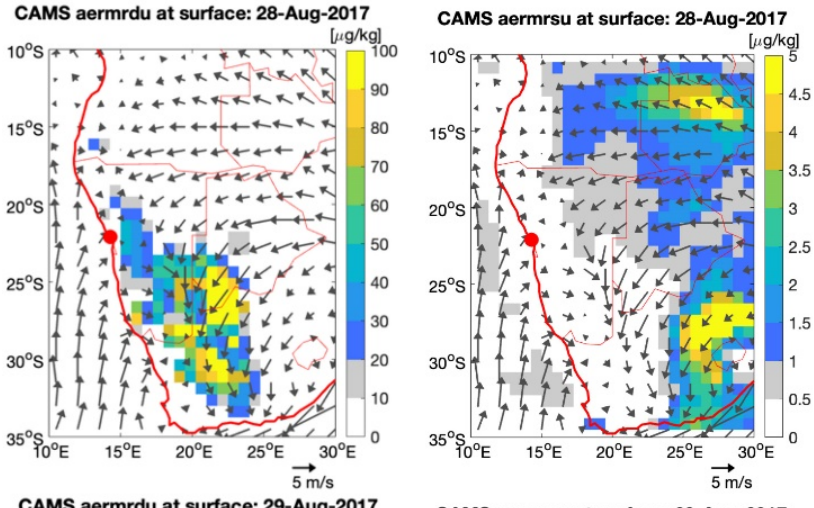
CAMS aermrdu at surface: 28-Aug-2017
[μg/kg]
100
90
80
70
60
50
40
30
20
10
0
10°S
15°S
20°S
25°S
30°S
35°S
10°E
15°E
20°E
25°E
30°E
5 m/s

CAMS aermrsu at surface: 28-Aug-2017
[μg/kg]
5
4.5
4
3.5
3
2.5
2
1.5
1
0.5
0
10°S
15°S
20°S
25°S
30°S
35°S
10°E
15°E
20°E
25°E
30°E
5 m/s

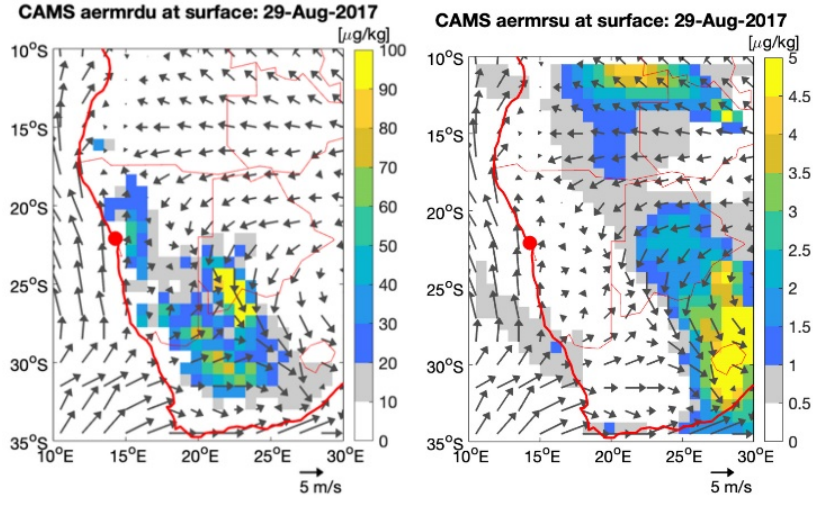
CAMS aermrdu at surface: 29-Aug-2017
[μg/kg]
100
90
80
70
60
50
40
30
20
10
0
10°S
15°S
20°S
25°S
30°S
35°S
10°E
15°E
20°E
25°E
30°E
5 m/s

CAMS aermrsu at surface: 29-Aug-2017
[μg/kg]
5
4.5
4
3.5
3
2.5
2
1.5
1
0.5
0
10°S
15°S
20°S
25°S
30°S
35°S
10°E
15°E
20°E
25°E
30°E
5 m/s

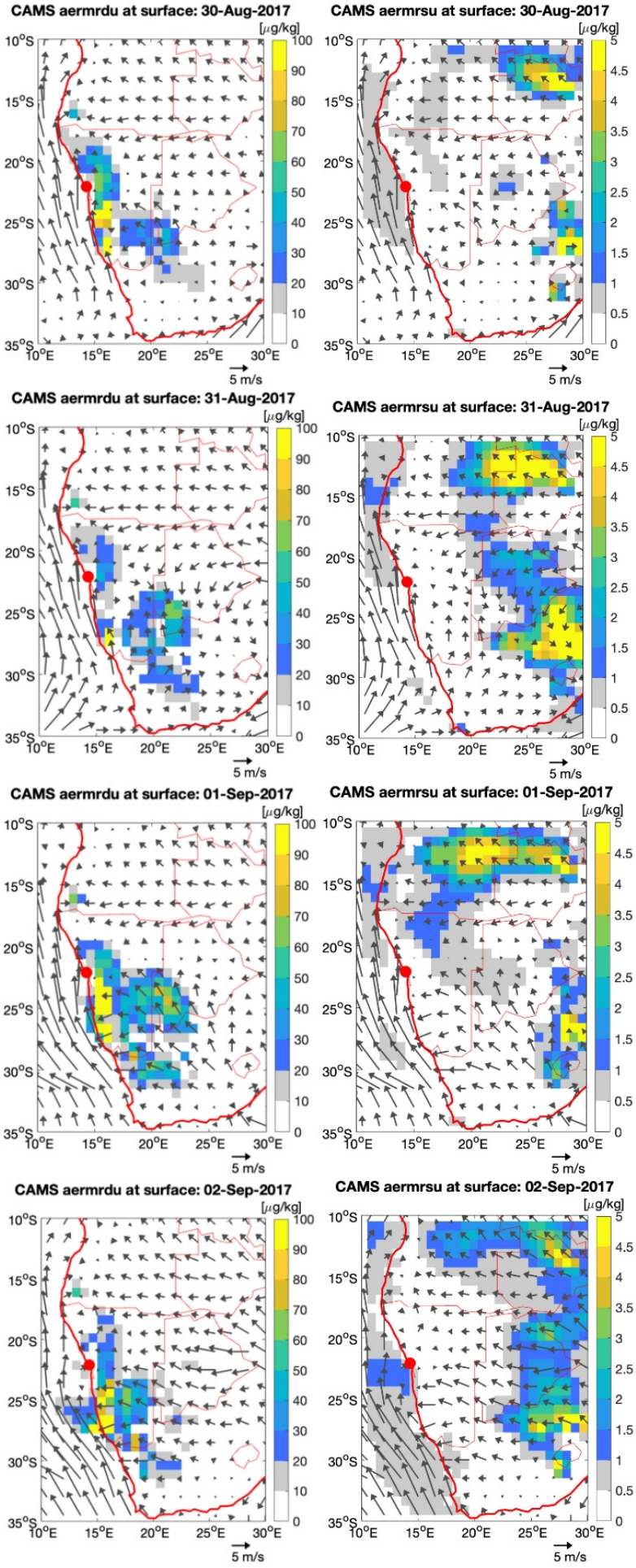
CAMS aermrdu at surface: 30-Aug-2017
CAMS aermrsu at surface: 30-Aug-2017
CAMS aermrdu at surface: 31-Aug-2017
CAMS aermrsu at surface: 31-Aug-2017
CAMS aermrdu at surface: 01-Sep-2017
CAMS aermrsu at surface: 01-Sep-2017
CAMS aermrdu at surface: 02-Sep-2017
CAMS aermrsu at surface: 02-Sep-2017
[μg/kg]
10°S
15°S
20°S
25°S
30°S
35°S
10°E
15°E
20°E
25°E
30°E
5 m/s

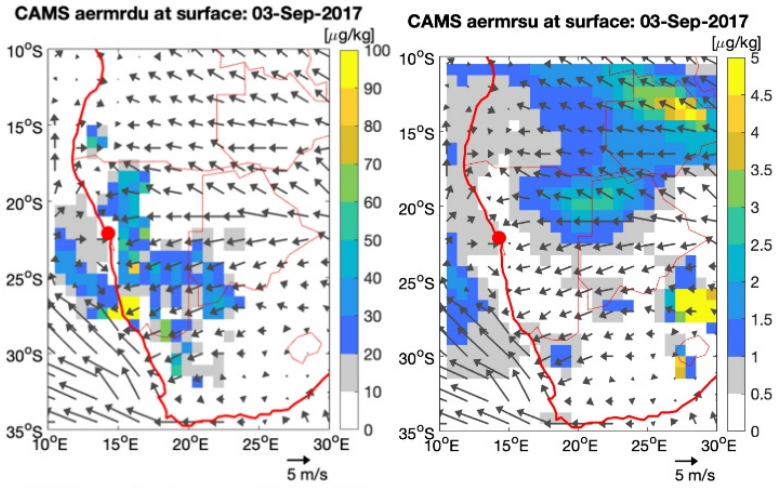
CAMS aermrdu at surface: 03-Sep-2017
[μg/kg]
CAMS aermrsu at surface: 03-Sep-2017
[μg/kg]
10°S
15°S
20°S
25°S
30°S
35°S
10°E
15°E
20°E
25°E
30°E
5 m/s

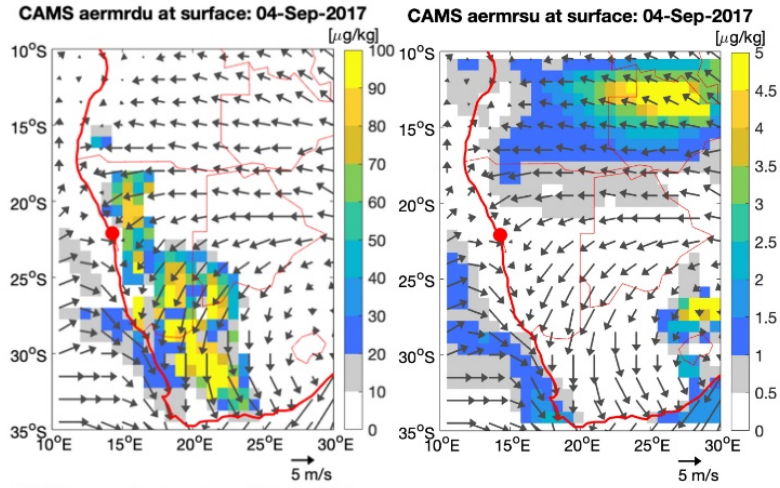
CAMS aermrdu at surface: 04-Sep-2017
[μg/kg]
CAMS aermrsu at surface: 04-Sep-2017
[μg/kg]
10°S
15°S
20°S
25°S
30°S
35°S
10°E
15°E
20°E
25°E
30°E
5 m/s

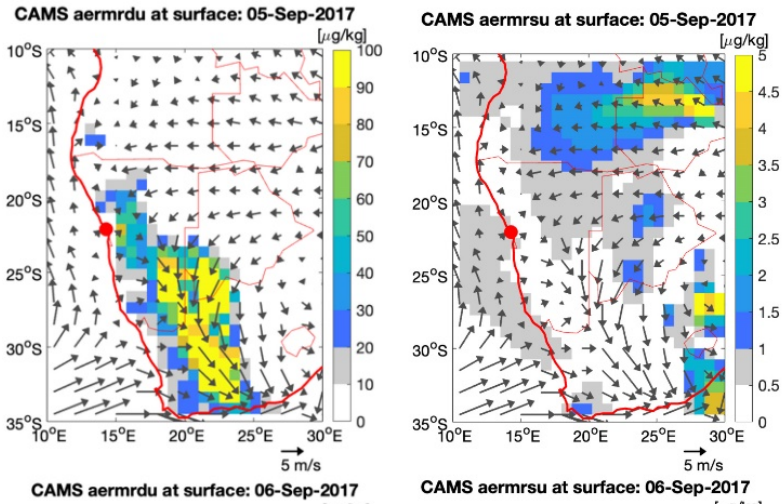
CAMS aermrdu at surface: 05-Sep-2017
[μg/kg]
CAMS aermrsu at surface: 05-Sep-2017
[μg/kg]
10°S
15°S
20°S
25°S
30°S
35°S
10°E
15°E
20°E
25°E
30°E
5 m/s

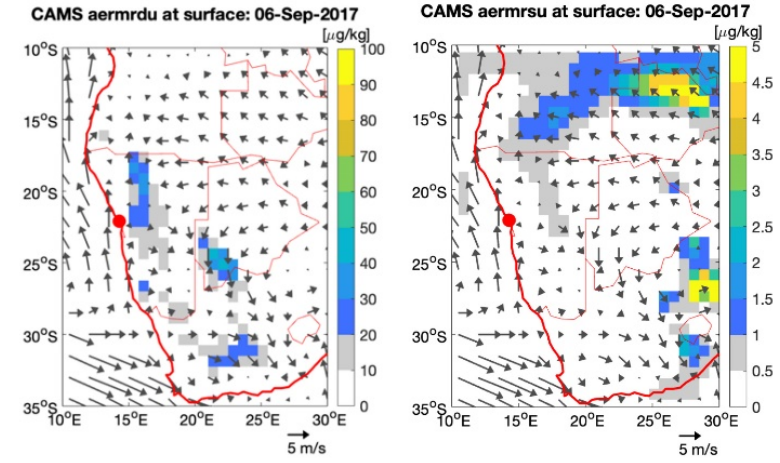
CAMS aermrdu at surface: 06-Sep-2017
[μg/kg]
CAMS aermrsu at surface: 06-Sep-2017
[μg/kg]
10°S
15°S
20°S
25°S
30°S
35°S
10°E
15°E
20°E
25°E
30°E
5 m/s

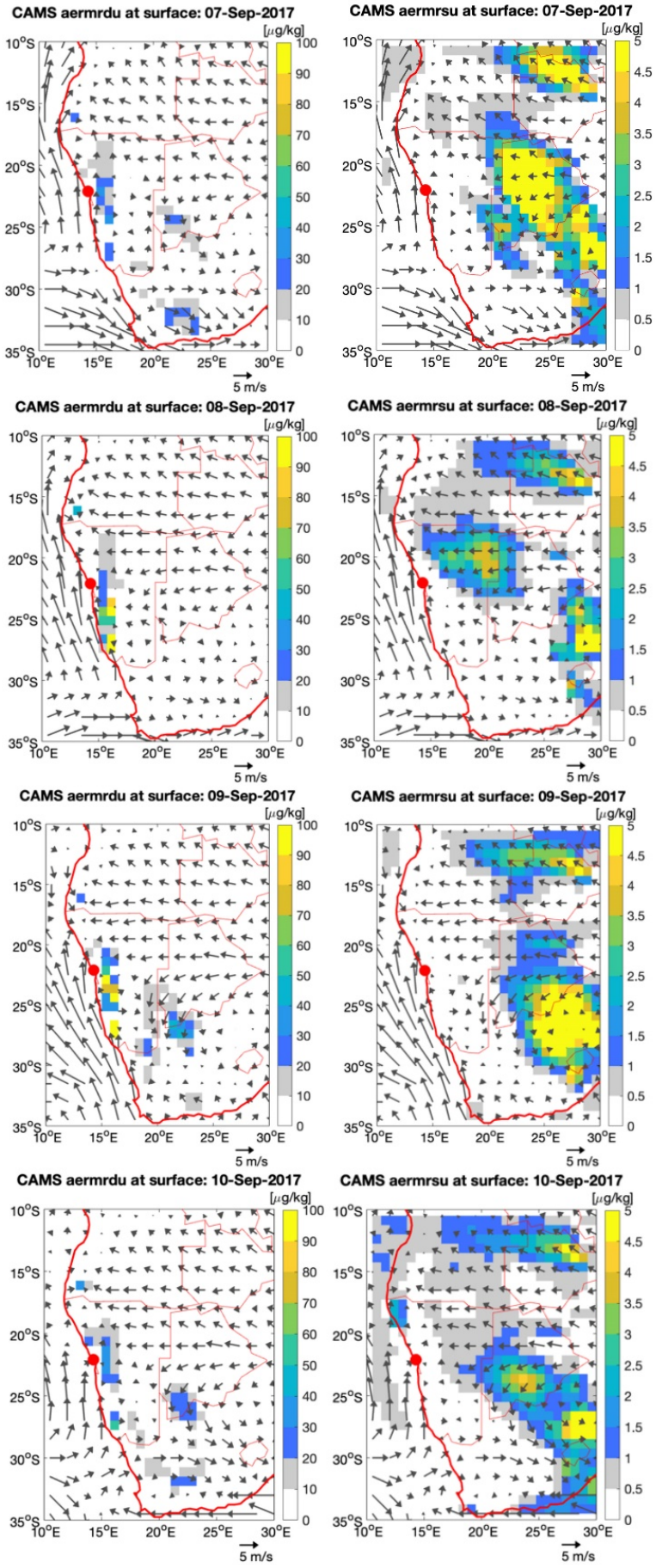
CAMS aermrdu at surface: 07-Sep-2017
CAMS aermrsu at surface: 07-Sep-2017
CAMS aermrdu at surface: 08-Sep-2017
CAMS aermrsu at surface: 08-Sep-2017
CAMS aermrdu at surface: 09-Sep-2017
CAMS aermrsu at surface: 09-Sep-2017
CAMS aermrdu at surface: 10-Sep-2017
CAMS aermrsu at surface: 10-Sep-2017
[μg/kg]
10°S
15°S
20°S
25°S
30°S
35°S
10°E
15°E
20°E
25°E
30°E
5 m/s

91

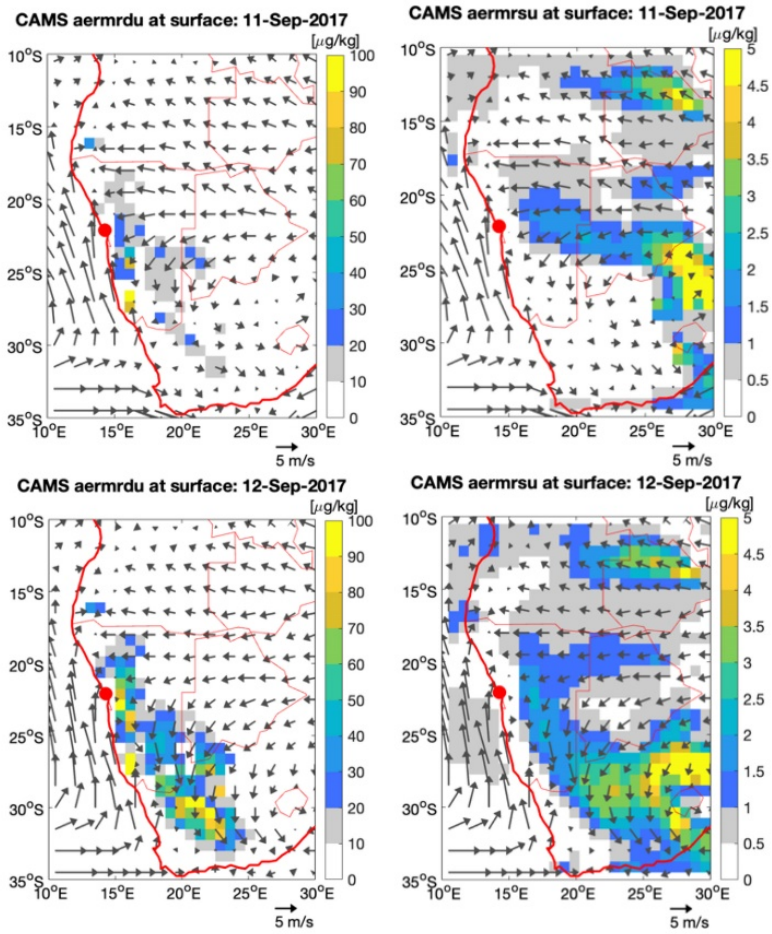
CAMS aermrdu at surface: 11-Sep-2017
[μg/kg]
100
90
80
70
60
50
40
30
20
10
0
10°S
15°S
20°S
25°S
30°S
35°S
10°E
15°E
20°E
25°E
30°E
5 m/s
CAMS aermrsu at surface: 11-Sep-2017
[μg/kg]
5
4.5
4
3.5
3
2.5
2
1.5
1
0.5
0
CAMS aermrdu at surface: 12-Sep-2017
CAMS aermrsu at surface: 12-Sep-2017

Figure S8. First derivative of the XANES normalized spectra measured during AEROCLO-sA (see Figure 5). The spectral positions of the absorption bands of Fe(II) and Fe(III) in the pre-edge region (7112.1 to 7117.8 eV) as well as those of illite (7128 eV) and various Fe(III) minerals, including hematite (7146 eV), according to Wilke et al. (2001) are indicated by vertical intermittent lines.

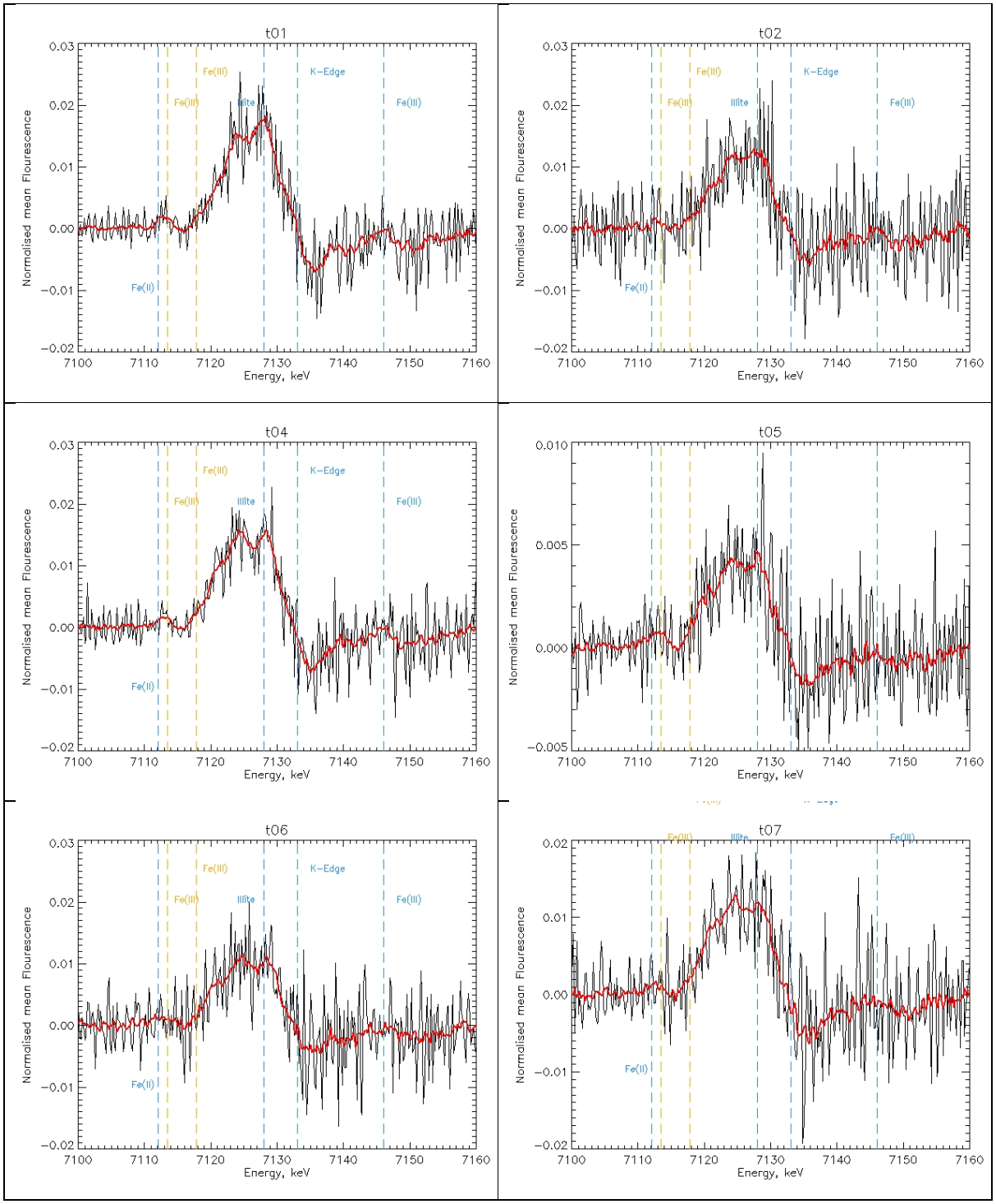

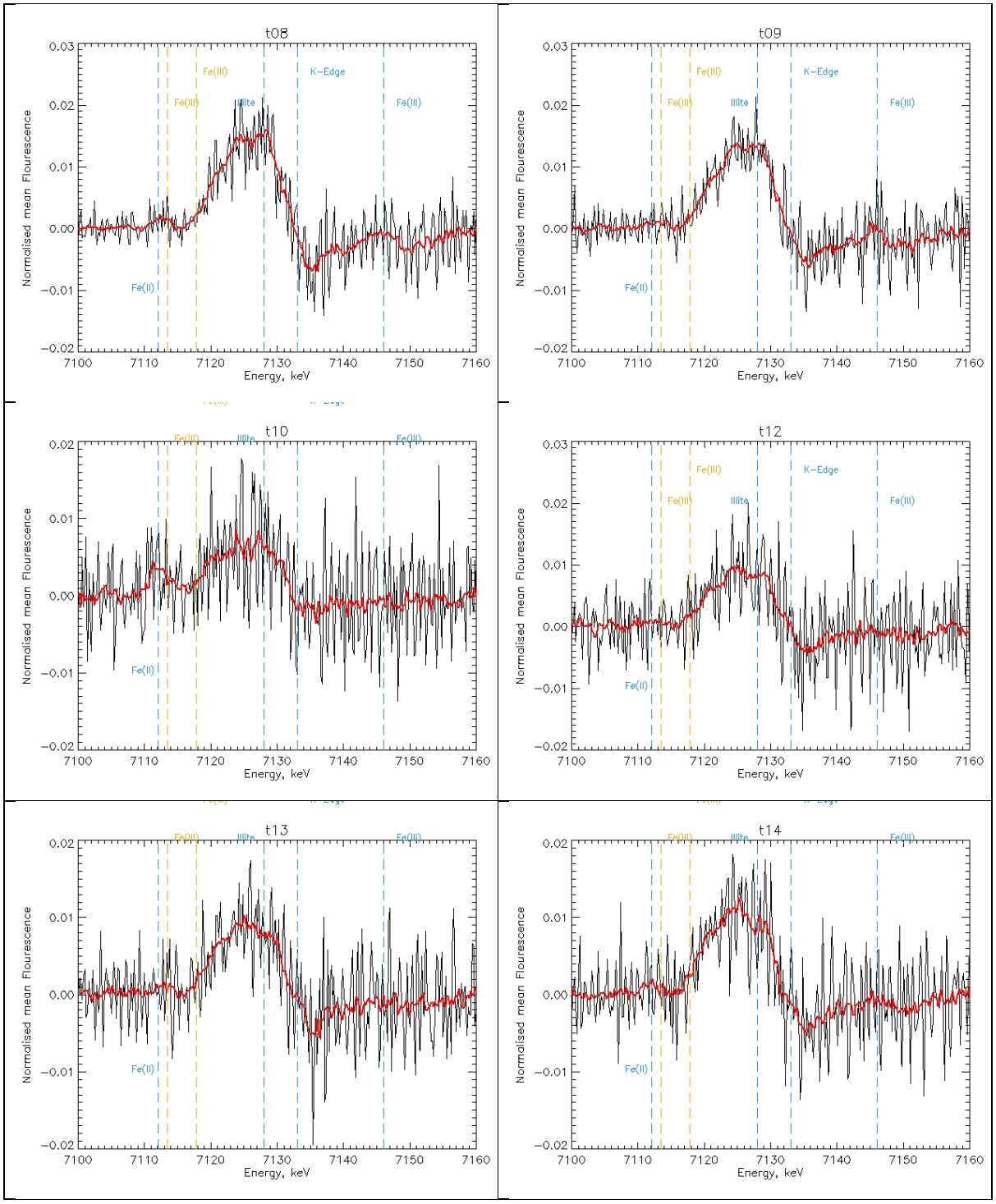
t08
t09
t10
t12
t13
t14
Fe(II)
Fe(III)
Illite
K-Edge
Normalised mean Flourescence
Energy, keV
7100
7110
7120
7130
7140
7150
7160
0.03
0.02
0.01
0.00
−0.01
−0.02

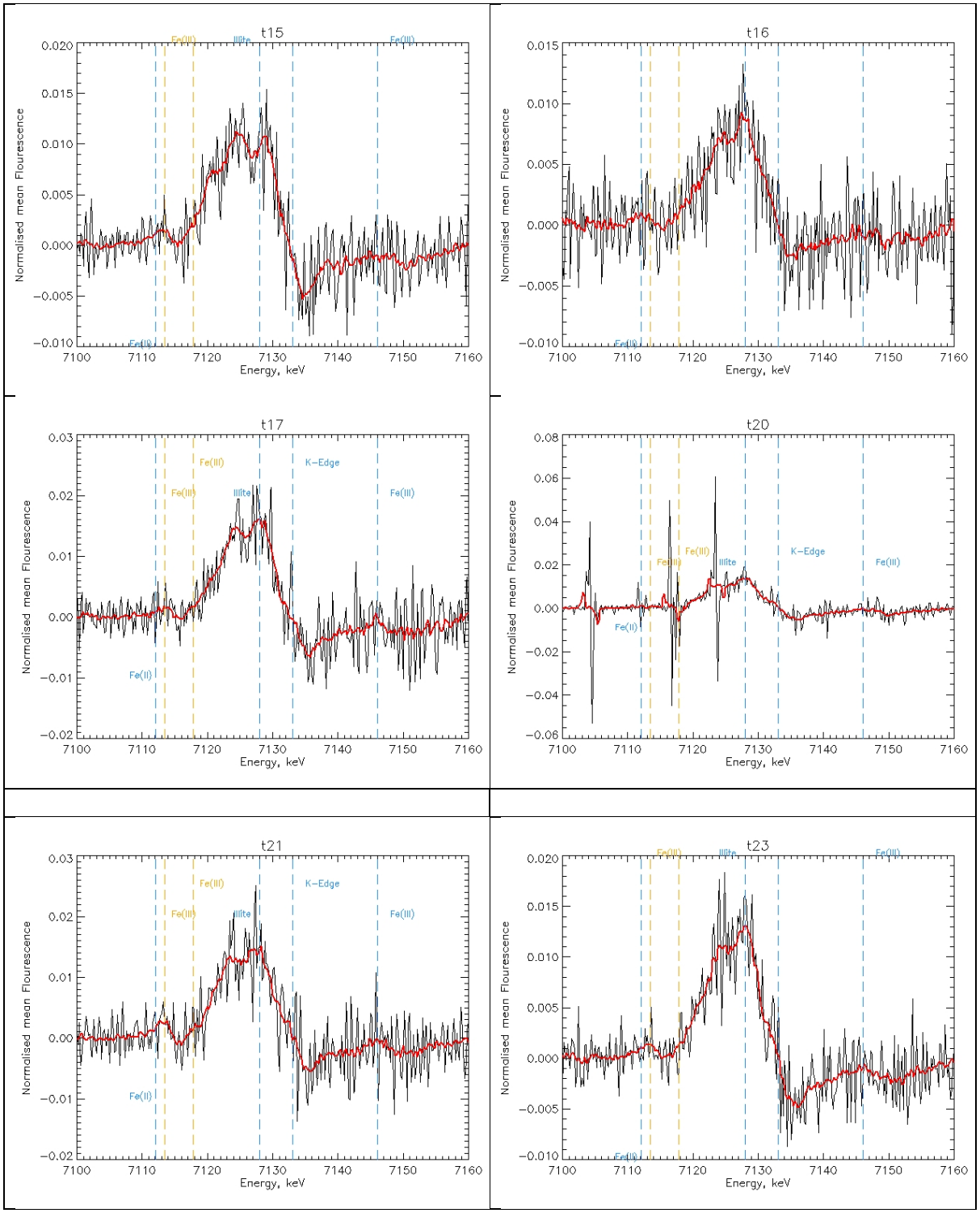
t15
t16
t17
t20
t21
t23
Normalised mean Flourescence
Energy, keV
Fe(II)
Fe(III)
Illite
K-Edge

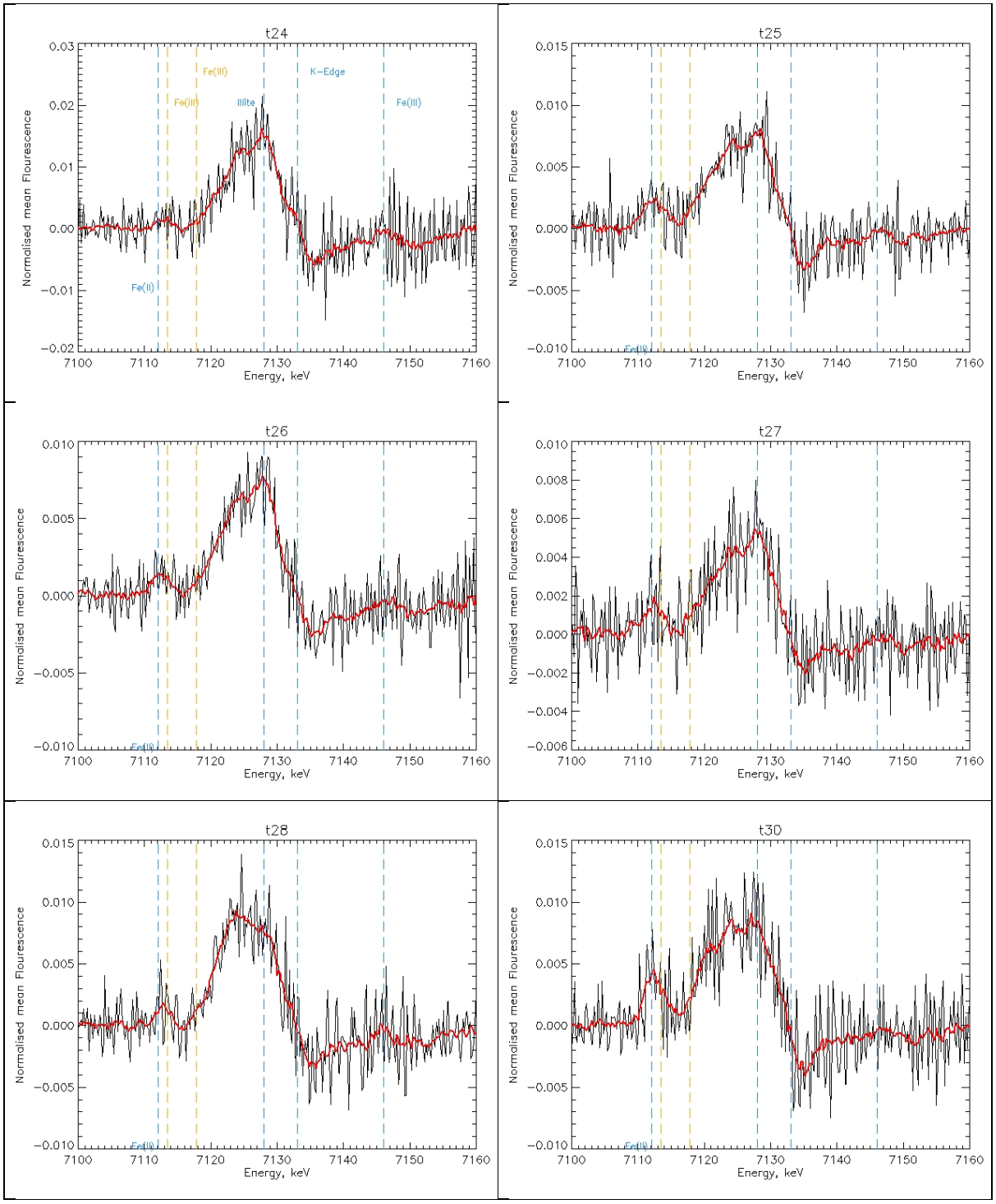
t24
Fe(III)
Fe(III)
Illite
K−Edge
Fe(III)
Fe(II)
Normalised mean Flourescence
Energy, keV
t25
Normalised mean Flourescence
Energy, keV
t26
Normalised mean Flourescence
Energy, keV
t27
Normalised mean Flourescence
Energy, keV
t28
Normalised mean Flourescence
Energy, keV
t30
Normalised mean Flourescence
Energy, keV

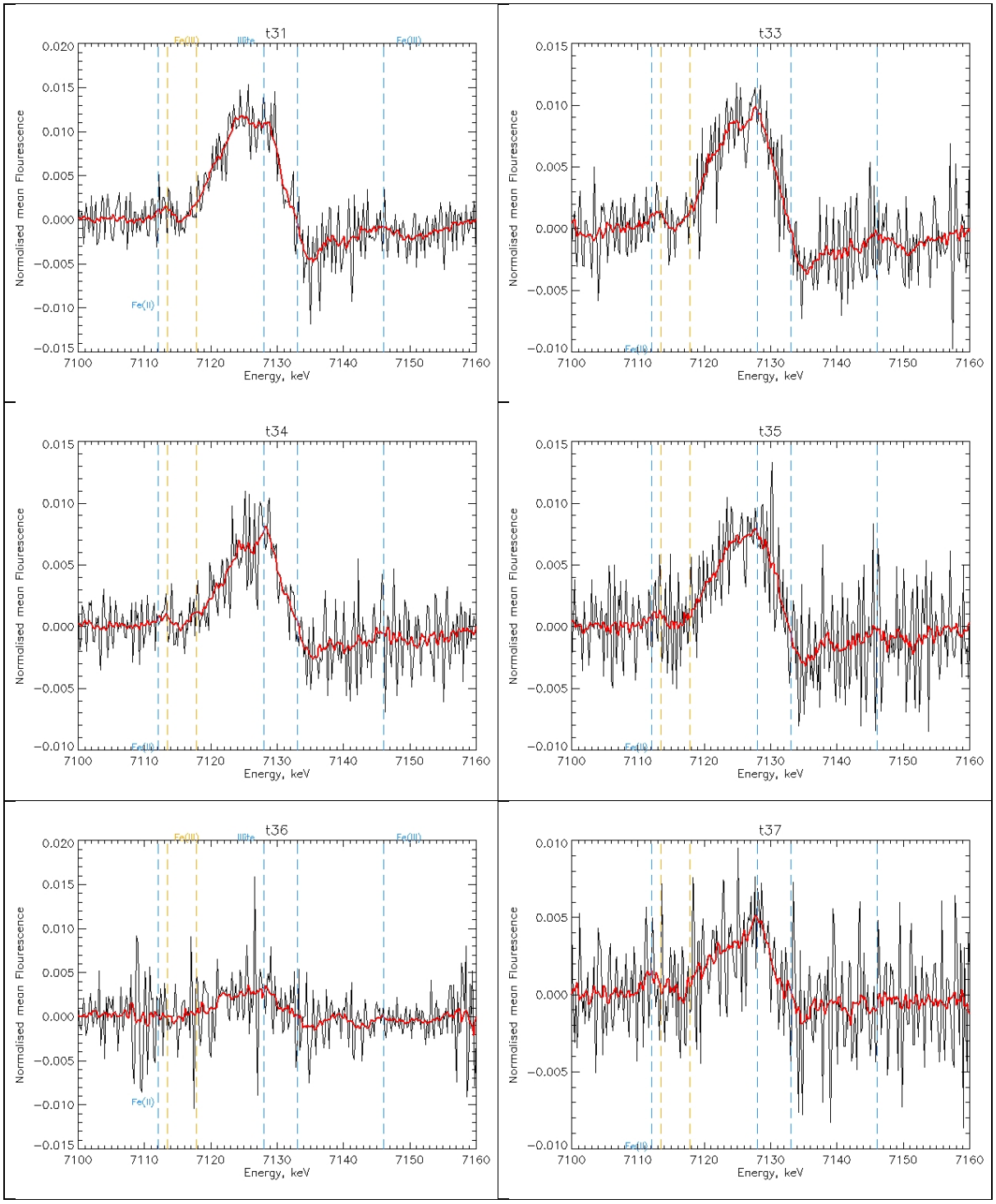
t31
t33
t34
t35
t36
t37
Normalised mean Flourescence
Energy, keV
Fe(II)
Fe(III)

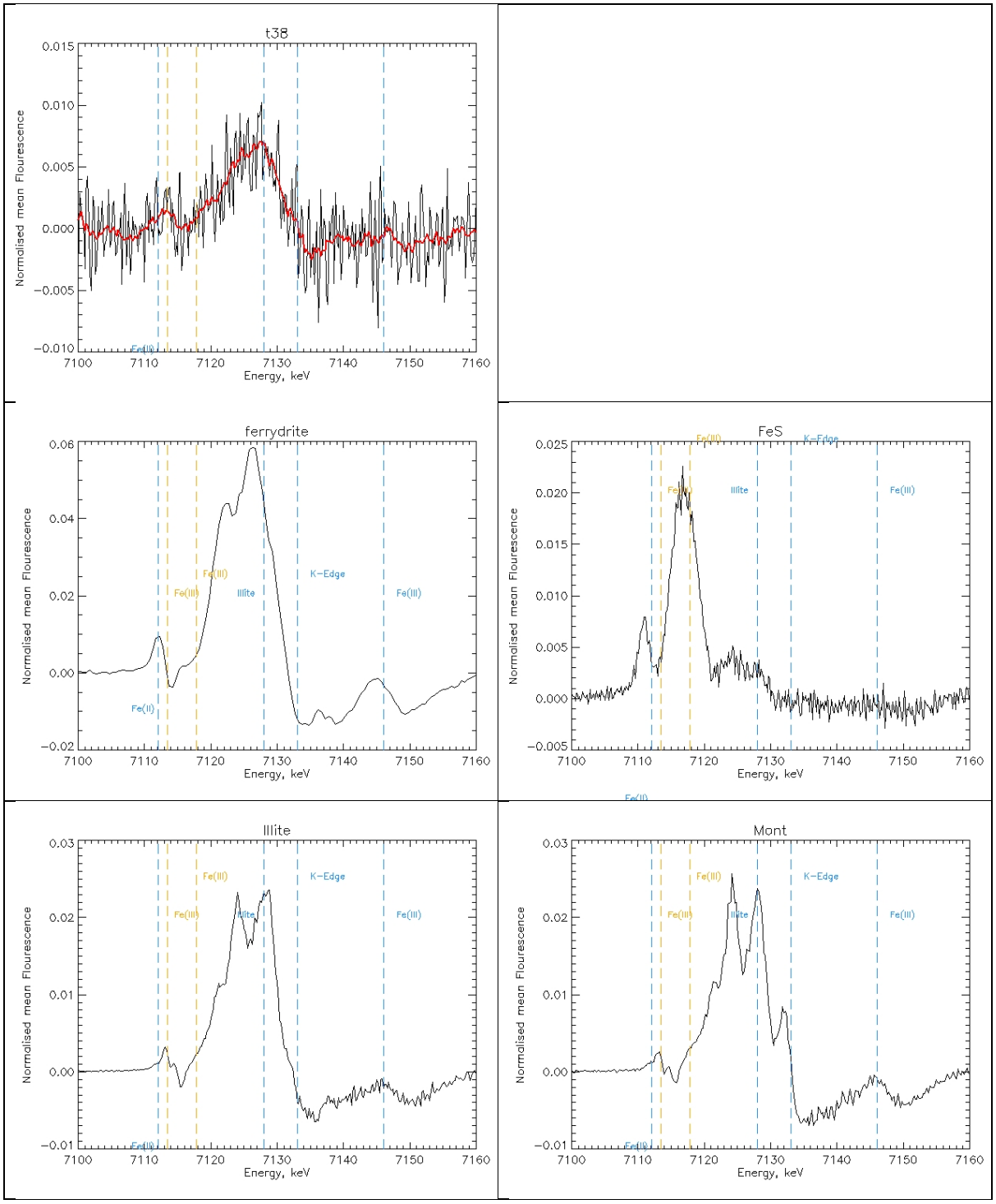
t38
Normalised mean Flourescence
Energy, keV
ferrydrite
Fe(II)
Fe(III)
Fe(III)
Illite
K-Edge
Fe(III)
FeS
Fe(III)
Illite
Fe(III)
Illite
Fe(III)
Fe(III)
K-Edge
Fe(III)
Mont
Fe(II)
Fe(III)
Illite
K-Edge
Fe(III)

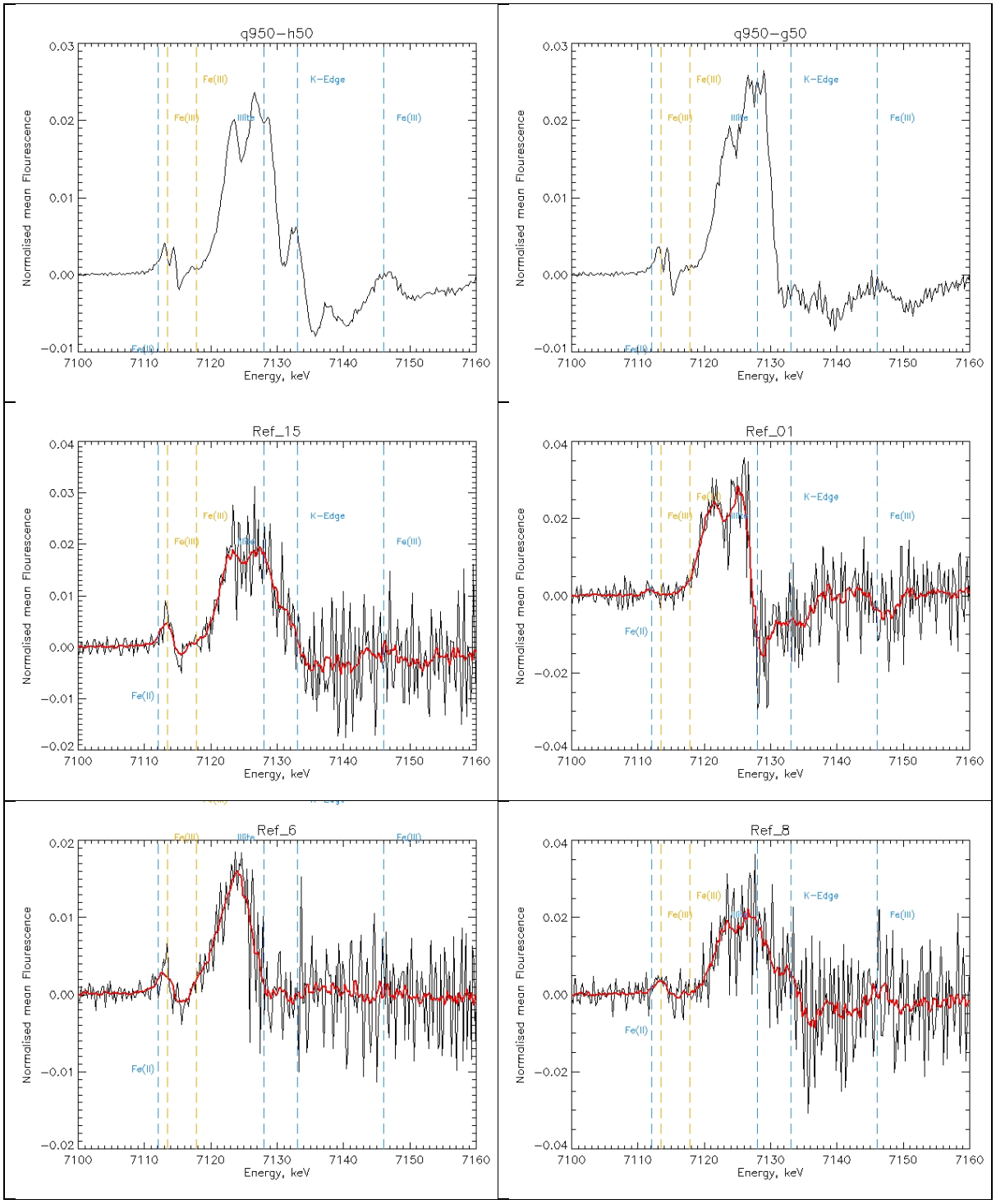
q950-h50
q950-g50
Ref_15
Ref_01
Ref_6
Ref_8
Normalised mean Flourescence
Energy, keV
Fe(II)
Fe(III)
K-Edge

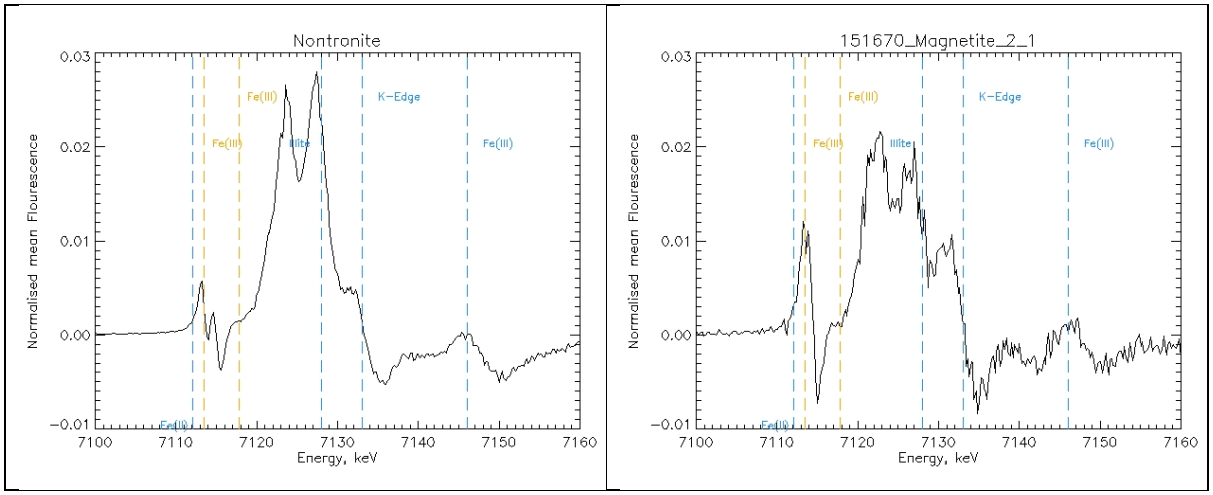
Nontronite
151670_Magnetite_2_1
Normalised mean Flourescence
Energy, keV
Fe(II)
Fe(III)
Illite
K-Edge
0.03
0.02
0.01
0.00
−0.01
7100
7110
7120
7130
7140
7150
7160

99
100

Figure S9. Box and whisker distributions of the fractional solubility of various elements during the field campaign. Values are sorted according to the meteorological periods P1 to P3. The P3 period is split into two sub-periods (P3a and P3b) to highlight the changes in the particle composition towards the end of the campaign. The box indicates the interquartile range, i.e. the 25th and 75th percentiles, and the line within the box marks the median. The whiskers indicate the quartiles 1.5 times the interquartile range. Points above and below the whiskers indicate outliers outside the 10th and 90th percentiles.

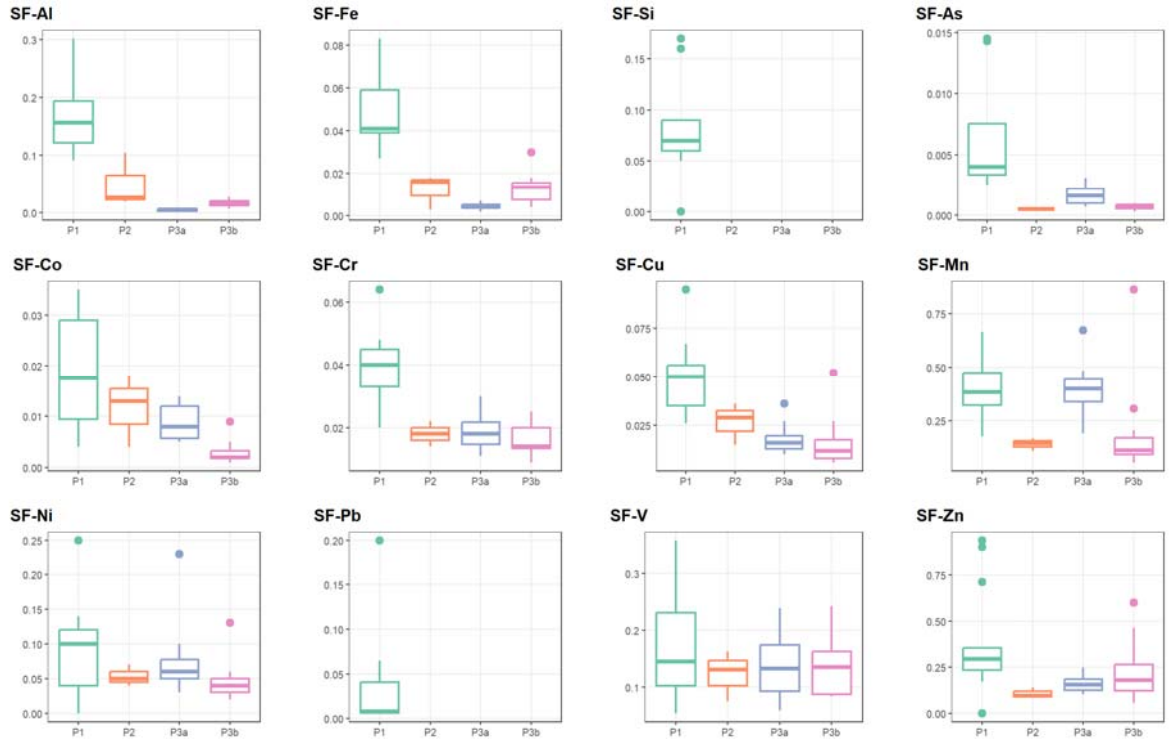

Text S1. Organic composition of aerosols

Due to low quantities of organic carbon measured during the campaign, the analysis of the composition of the organic fraction was done on extracts representing the combination of filter samples available for the P1 (T9, T12, T13 and T14), P2 (T17, T20, T21, T22, and T23) and P3 (T31, T32, T33, T38) periods. The results of formulae assignment for water soluble organic carbon (WSOC) from three samples representing a shift from P1 to P3 time ranges are depicted in Figure S10 as van Krevelen diagrams, absolute numbers, and intensity contributions of CcHhOoNnSs assignments.

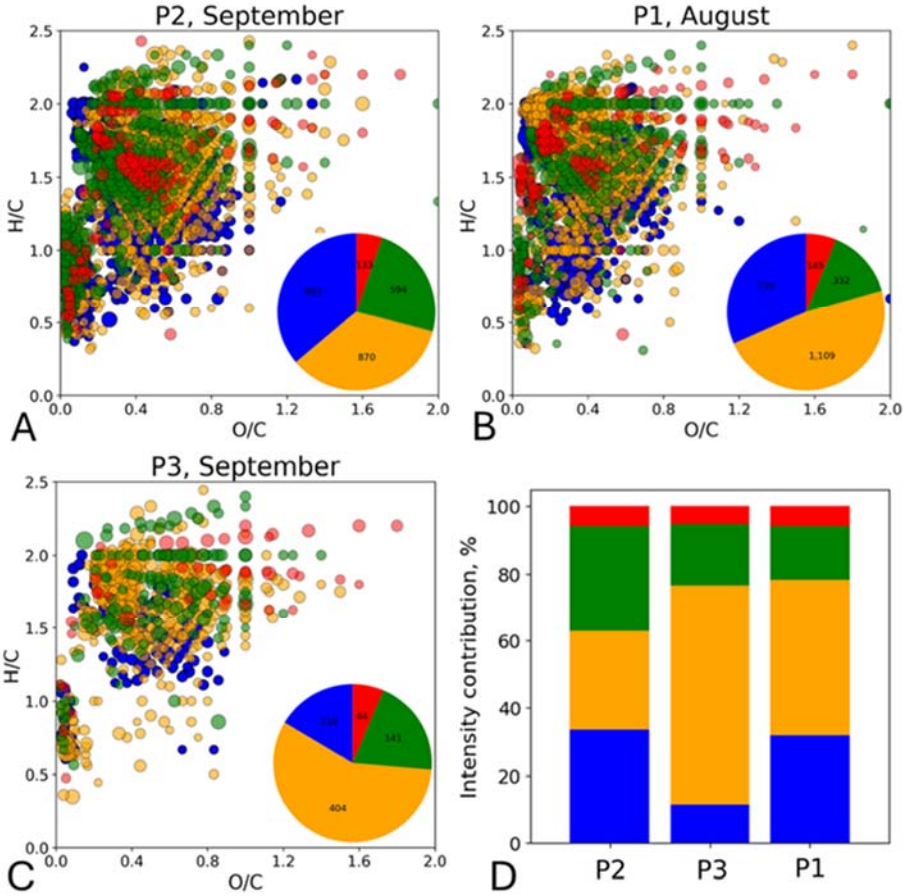

Figure S10. Van Krevelen diagrams (A, B, C) and formulae intensity contribution (D) for WSOC isolated from P1-P3 aerosols. Pie-charts indicate the number of CHO, CHON, CHOS and CHONS assignments, colour-coded in blue, orange, green and red, respectively.

A total number of 2321, 2500, and 705 molecular formulae were assigned for the P1, P2, and P3 samples, respectively, with 375 common formulae between the three. In all cases, the number of assigned formulae per elemental group decreased in the following order: CHON>CHO>CHOS>CHONS, which is typical for organic aerosols. The number and intensity contribution of CHOS formulae were higher in P2 samples compared to other periods: 31% in P2 vs 16 and 18 in P1 and P3, respectively, with 116 common CHOS formulae between the

three periods. The number of CHON formulae was highest in the P1 sample: 1109 vs. 870 and 404 for P2 and P3, respectively. At the same time intensity contribution of CHON species was highest for P3. Visual inspection of van Krevelen diagram shows the dominant contribution of saturated and unsaturated compounds with H/C > 1 in all cases.

Plotting double bond equivalent (DBE) vs molecular mass (M) diagram provides additional insights on the unique molecular features of P1, P2 and P3 periods by showing the connection between mass and unsaturation degree (Figure SS11). For a deeper interpretation, the colour bar has been added designating the number of oxygen atoms in molecular formulae.

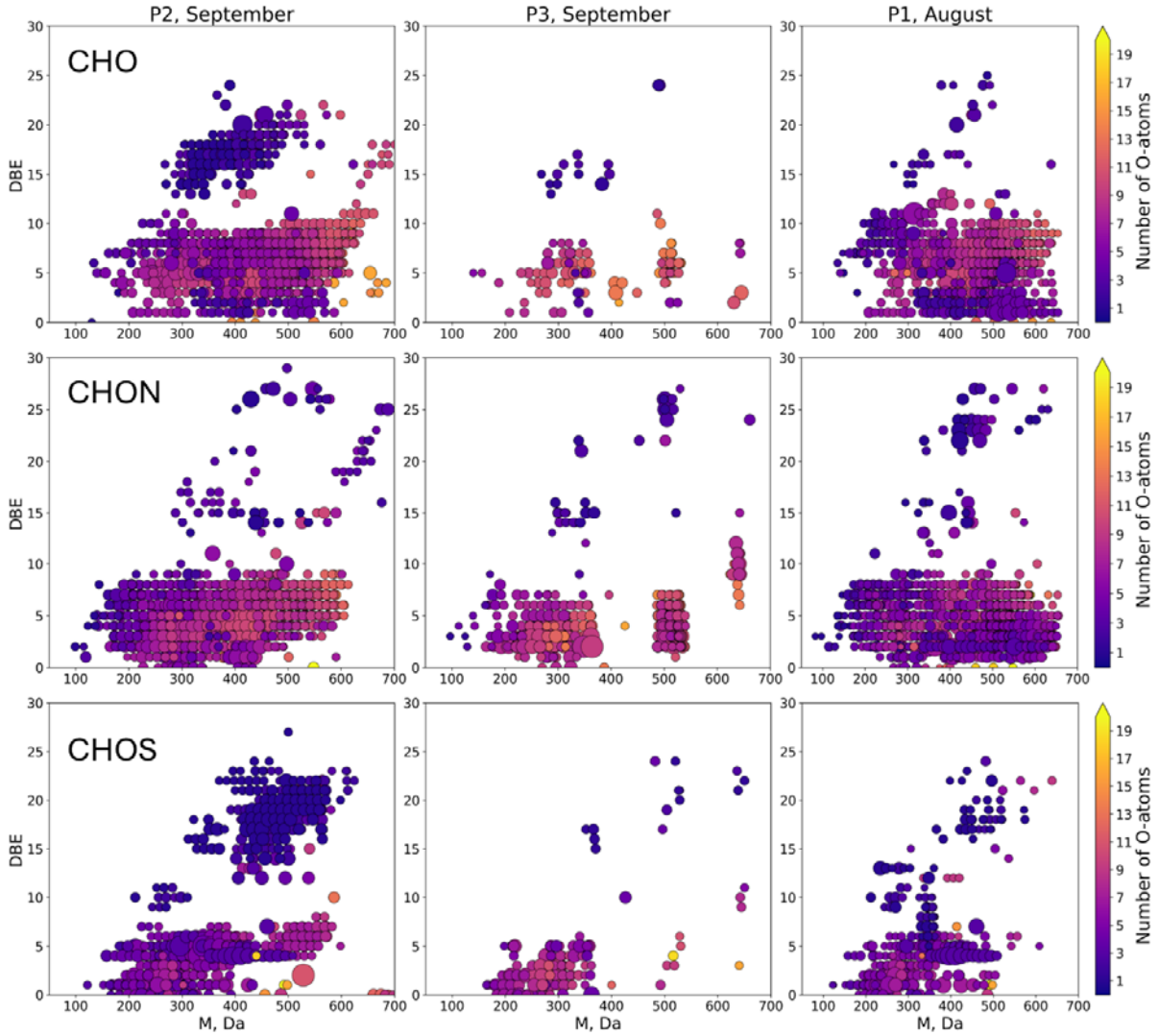

Figure S11. DBE vs M diagrams for CHO, CHON and CHOS compounds of WSOC from P3 (left panel) and P2 (right panel) samples. Color bars designate the number of oxygen atoms in molecular formulae.

In all cases, most of the compounds were characterized by DBE values below 10 and a mass range from 100 to 700 Da. Medium and high-molecular-weight CHO compounds with DBE below 5 were detected in all samples. Yet, in the case of P1, these compounds were low

oxidized with a number of O-atoms below 5 while in the case of P2 and P3 this region of the diagram was occupied by highly oxygenated compounds. P1 sample also included highly saturated low-oxidized compounds with molecular mass around 100 Da, which were missing from P2 and P3. P1 was also distinct by the presence of high-molecular-weight low-oxidized CHON compounds. Together with CHO compounds, this likely indicates a higher contribution of biogenic emission on WSOC during P1. Peculiarity of P2 sample was in the abundance of two families of CHO and CHOS compounds clearly depicted in Figure S8. The P2 sample included middle-mass range highly unsaturated compounds with DBE > 15. In both CHO and CHOS cases, these compounds were low-oxygenated. Together with van Krevelen diagrams the observed molecular features likely indicate the increase in the contribution of burning aerosols in P2 as compared to P1 period which is aligned with the air mass origin. In addition, WSOC from P2 included relatively saturated oxidized S-containing compounds with molecular masses above 500 Da and DBE values below 10, which might indicate the contribution of sulfate-enriched dust from smelting. The abrupt increase in the contribution of CHOS compounds together with the distinct appearance of new highly unsaturated compounds, supports the hypothesis on the stronger influence of anthropogenic activities on aerosol chemical composition in September.

Text S2. Results of PMF analysis

The PMF analysis extracted four factors. As expected, "sea spray" is the dominant factor with a concentration of up to 135.1 μg m^{-3} (Table S5), contributing on average to 45.7% of the PM mass (Figure S12).

Table S5. Descriptive statistics of PMF factor scores in μg m^{-3} (N = 35).

	mean	St.dev	median	max	75th perc	25th perc	min
Si-rich	22.7	23.6	14.6	81.5	43.2	0.8	0.0
Mineral Dust	3.8	3.7	2.9	11.4	7.3	0.6	0.0
Sea Spray	39.2	29.5	37.0	135.1	60.8	18.6	0.0
Secondary Aerosol	18.5	15.1	14.5	50.2	24.7	9.9	0.0

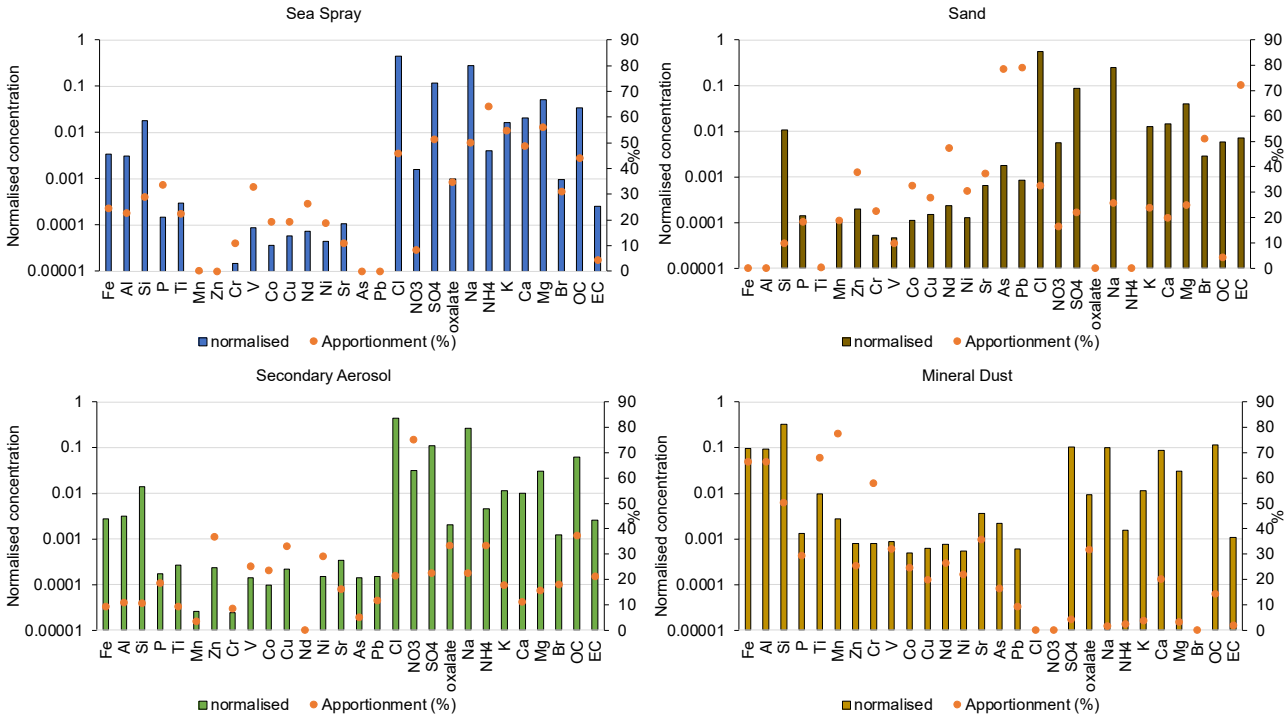

Figure S12. Results of the PMF analysis applied to TSP chemical composition. Bars show the normalised profiles (loadings) of the PMF factors (in log-scale) and dots show the apportionment (in %) of each chemical species to each factor.

The PMF "sea spray" component was represented by high loadings of Na^+, Cl^-, Mg^{2+}, SO_4^{2-} and OC (Figure). It peaked during the initial part of the campaign and when winds blew from the ocean.

The second most dominant factor is "secondary aerosol", contributing on average to 25.2% of the PM mass (Figure S12). This factor is characterised by high loadings of NO_3^-, SO_4^{2-}, oxalate, and NH_4^+, as well as OC. It is characterised also by high loadings of Na^+ and Cl^- but an anti-correlation with the sea spray factor (r = -0.44), so rather than being a purely secondary aerosol factor it can be considered as aged sea spray. Its contribution increases toward the second part of the campaign, and it is generally higher during the day, due to enhanced photo-oxidation (Figure S12). The sea spray and secondary aerosol factors presented the following

ratios: SO_4^{2-}/Na^+ = 0.420, K^+/Na^+ = 0.059, and Ca^{2+}/Na^+ = 0.073 and SO_4^{2-}/Na^+ = 0.408, K^+/Na^+ = 0.042, and Ca^{2+}/Na^+ = 0.037, respectively. The values are closer to the measured values in sea water collected on site (Giorio et al., submitted) rather than literature values (Formenti et al., 2002; Klopper et al., 2020). These two factors were also extracted for PM_1 (not shown). In the case of PM_1, the anti-correlation of these two factors is stronger than in TSP (r = -0.72 in PM_1, r = -0.44 in TSP).

Two factors characterised by a high loading of metals were identified: "Si-rich" accounting for 23.3% of PM mass and "mineral dust" accounting for 5.8% of PM mass (Figure S13). The "Si-rich" factor extracted from this dataset is different from both the "fugitive dust" and the "industry" factor extracted by Klopper et al. (2020) on a dataset covering a longer period over the years 2016-2017 and based on PM_{10} samples collected on a rooftop terrace of the HBAO station. The "Si-rich" factor extracted in this study is characterised by the presence of a high loading of Si but not associated with Al and Fe, contrarily to what can be observed for mineral dust. It is also characterised by high loadings of As and Pb, which are strongly correlated to each other (r=0.97), as well as moderate loadings of Co, Cu, Ni, Nd, Sr and Zn (Figure). In addition, EC is predominantly present in this factor as well as a marine signature (e.g., Na^+, Cl^-, and other species observed in the sea spray factor). The "Si-rich" factor was not observed in PM_1.

The mineral dust factor is characterised by high loadings of Al, Fe, and Si, as well as Ti, Mn, Na^+, Ca^{2+}, and SO_4^{2-} (Figure S13).

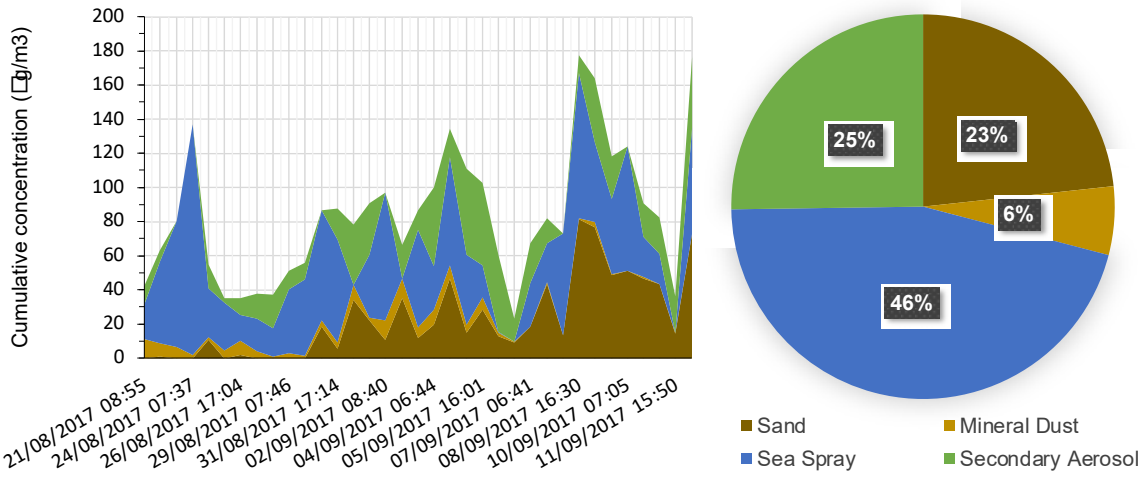

Figure S13. Timeseries (scores) of the PMF factors obtained from the PMF analysis applied to TSP chemical composition (a) and average apportionment of TSP concentration during the campaign (b). Dates are reported as "DD/MM/YYYY hh:mm".

Its contribution increases during the central part of the campaign with winds showing an easterly component. The mineral dust contribution remains however moderate throughout the campaign as no significant dust episode occurred during the campaign.

Note that fluoride was not included in the PMF analysis because its concentrations were below detection limit for almost half of the campaign.

References of supplementary material

Michalowicz, A., Moscovici, J., Muller-Bouvet, D., and Provost, K.: MAX: Multiplatform Applications for XAFS, Journal of Physics Conference Series (Online), 190, 4, Doi:101088/1742-6596/190/1/012034, 2009.